Available online at www.sciencedirect.com

ScienceDirect

Geochimica et Cosmochimica Acta 283 (2020) 103–123

Geochimica et Cosmochimica Acta

www.elsevier.com/locate/gca

Petrogenesis, alteration, and shock history of intermediate shergottite Northwest Africa 7042: Evidence for hydrous magmatism on Mars?

T.V. Kizovski [a,b,*], M.R.M. Izawa [a,1], K.T. Tait [a,b], D.E. Moser [c], J.M.D. Day [d], B.C. Hyde [a,c], L.F. White [a,b], L. Kovarik [e], S.D. Taylor [f], D.E. Perea [e], I.R. Barker [c], B.R. Joy [g]

[a] *Centre for Applied Planetary Mineralogy, Department of Natural History, Royal Ontario Museum, 100 Queen's Park, Toronto, Ontario M5S 2C6, Canada*

[b] *Department of Earth Sciences, University of Toronto, 22 Russell Street, Toronto, Ontario M5S 3B1, Canada*

[c] *Department of Earth Sciences, University of Western Ontario, London, Ontario N6A 5B7, Canada*

[d] *Scripps Institution of Oceanography, University of California San Diego, La Jolla, CA 92093-0244, USA*

[e] *Environmental Molecular Sciences Laboratory, Pacific Northwest National Laboratory, Richland, WA 99352, USA*

[f] *Physical and Computational Sciences Directorate, Pacific Northwest National Laboratory, Richland, WA 99352, USA*

[g] *Department of Geological Sciences and Geological Engineering, Queen's University, Kingston, Ontario K7L 3N6, Canada*

Received 23 August 2019; accepted in revised form 27 May 2020; available online 4 June 2020

Abstract

Northwest Africa (NWA) 7042 is an intermediate, permafic shergottite consisting of two generations of olivine (early zoned olivine Fo_{41-76}, and late-stage fayalitic olivine Fo_{46-56}), complexly zoned pyroxene ($En_{35-64}Fs_{22-46}Wo_{5-34}$), shock-melted or maskelynitized feldspar ($An_{5-30}Ab_{16-61}Or_{1-47}$), and accessory merrillite, apatite, ilmenite, titanomagnetite, Fe-Cr-Ti spinels, pyrrhotite, and baddeleyite. The zoned olivine grains have been pervasively modified, containing conspicuous brown Mg-rich cores surrounded by colorless, unaltered Fe-rich overgrowth rims. This textural relationship suggests that the cores were altered at magmatic temperatures prior to crystallization of the rims on Mars. Launch-generated shock veins in NWA 7042 also crosscut and displace several of the altered olivine grains indicating that alteration occurred before ejection of the meteorite. While this type of olivine alteration is rare in shergottites, it is similar to deuterically altered olivine in basalts and gabbros on Earth, caused by residual water-rich magmatic fluids. Transmission electron microscopy analysis of the olivine alteration did not reveal the high-temperature phases expected from this process; however, NWA 7042 has also been subjected to extensive terrestrial weathering, which may explain their absence. The potential presence of deuterically altered olivine in NWA 7042 has significant implications, as it is the third martian meteorite where deuteric alteration of olivine has been observed (the others being NWA 10416, and Allan Hills 77005). The different mantle sources for the parental melts of these three meteorites would suggest many, if not all martian mantle reservoirs have the potential to produce water-rich magmas.

Keywords: NWA 7042; Shergottites; Mars; Shock processes; Intermediate compositions; Alteration

* Corresponding author at: Centre for Applied Planetary Mineralogy, Department of Natural History, Royal Ontario Museum, 100 Queen's Park, Toronto, Ontario M5S 2C6, Canada.

E-mail address: t.kizovski@mail.utoronto.ca (T.V. Kizovski).

[1] Present address: Institute for Planetary Materials, Okayama University, Misasa, Tottori 682-0193, Japan.

https://doi.org/10.1016/j.gca.2020.05.030

1. INTRODUCTION

Shergottites are the most common type of martian meteorite recovered to date and have mineralogical and petrological features similar to terrestrial mafic to ultramafic extrusive or hypabyssal igneous rocks (e.g., McSween and Treiman, 1998; Nyquist et al., 2001; Treiman, 2003). Shergottites can be divided into three subgroups based on their petrographic features: basaltic, olivine-phyric, or poikilitic (previously referred to as "lherzolitic"; Walton et al., 2012; McSween Jr., 2015); and can be further subdivided into geochemical groups (depleted, enriched, or intermediate variants) based on their incompatible trace element (ITE) abundances and lithophile isotope systematics (i.e., depleted = low La/Yb, $^{87}Sr/^{86}Sr < 0.712$; enriched = high La/Yb, $^{87}Sr/^{86}Sr > 0.712$; see Tait and Day, 2018 for a recent update). Several hypotheses have been proposed to explain the geochemical diversity among shergottites, including mixing of a depleted mantle source with an oxidized, enriched crust (Wadhwa, 2001; Herd et al., 2002). Recent geochemical studies have shown that this mixing model is unable to generate the observed ^{143}Nd-^{187}Os (Brandon et al., 2012) and coupled ^{187}Os-^{87}Sr isotope compositions of shergottites (Tait and Day, 2018). The trends between these isotope systems (and other comprehensive major and trace element analyses; Borg and Draper, 2003; Shearer et al., 2008; Shearer et al., 2013) are best explained by mixing of two distinct ancient mantle reservoirs, or deep melts and metasomatized martian lithosphere (Tait and Day, 2018; Day et al., 2018). Detailed analyses of newly discovered shergottites are needed to provide further constraints on these source reservoirs and mixing dynamics in Mars, as well as to advance our understanding of martian igneous processes.

Here, we report the detailed petrology, mineralogy, alteration, and shock features in intermediate permafic shergottite Northwest Africa (NWA) 7042. Geochemically, it is intermediate in ITE, reflecting a transitional stage between ITE-depleted primary melts, and more evolved ITE-enriched magmas (Day et al., 2018). It is also petrographically 'intermediate' between coarse-grained basaltic and olivine-phyric shergottites. The sample has some textural similarities to basaltic shergottites NWA 480/1460 and NWA 5029, but differs in abundance of olivine (Barrat et al., 2002; Connolly et al., 2008). It is also somewhat similar to NWA 2646, but NWA 2646 has a poikilitic texture with abundant chadocrysts of olivine, augite and chromite enclosed in larger oikocrysts of zoned pigeonite (Irving et al., 2012). The cosmic-ray exposure (CRE) age reported for NWA 7042 is within the range of the majority of basaltic shergottites (2–4 million years (m.y.); Usui et al., 2010) with exposure ages for noble gas chronometers ^{3}He, ^{21}Ne, and ^{38}Ar being reported at 2.4, 2.8, and 1.6 m.y., respectively (Huber et al., 2013).

NWA 7042 also contains unique alteration features distinct from most other shergottites. The cores of the olivine grains within the sample have been pervasively modified resulting in orange-brown stained cores with dark-brown margins, surrounded by yellow to colorless rims (possible overgrowths). The modified cores do not resemble typical olivine alteration in martian meteorites (i.e. iddingsite veins characterized within nakhlites), but do look similar to high-temperature iddingsite within some terrestrial basalts and gabbros caused by residual water-rich magmatic fluids (Ross and Shannon, 1925; Edwards, 1938; Goff, 1996; Caroff et al., 2000; Clément et al., 2007; Tschegg et al., 2010; Vaci et al., 2020). A similar alteration texture has been observed in one other shergottite (olivine-phyric NWA 10416; Vaci et al., 2020). Preliminary petrographic and geochemical studies of the alteration features in NWA 10416 point to a martian origin for the olivine alteration (Herd et al., 2016; Vaci et al., 2020). However, the alteration histories of both NWA 10416 and NWA 7042 are complicated due to the presence of terrestrial calcite/barite weathering veins that crosscut the olivine grains and are found throughout the samples. A range of oxygen isotope signatures within the olivines complicates this further (Piercy et al., 2020).

To date, petrographic and *in-situ* studies on NWA 7042 are limited to a few abstracts (Irving et al., 2012; Huber et al., 2013; Izawa et al., 2015). As such, the purpose of this work is to complete a detailed mineralogical, petrological, and geochemical analysis of NWA 7042 in order to better characterize its petrogenesis and subsequent alteration. As the timing of the alteration in NWA 7042 is of particular interest, this study includes a detailed discussion of the relationships between shock features and the altered olivine grains and examines the possibility of both terrestrial and martian formation mechanisms. A detailed description of the shock effects in maskelynite, baddeleyite, shock veins, and high-pressure phases is also presented.

2. SAMPLES AND METHODS

This study used the main mass of NWA 7042 (2.98 kg), which is housed at the Royal Ontario Museum (ROM) in Toronto, Canada (catalogue number M56450). Prominent features of the main mass include a dark brown outer surface of desert varnish, a thin (~1–10 mm) zone of pale weathering products (e.g. calcite) just below the brown varnish, and a network of dark shock veins visible as dark linear features crossing the sawn face of the sample (Fig. 1).

Two polished thin sections and a polished thick slab (~2 mm thickness) were prepared and analyzed for this study. An additional interior fragment devoid of fusion crust or terrestrial weathering was used for whole-rock analysis.

2.1. Optical petrography

Thin sections of NWA 7042 were examined in transmitted plane, crossed-polarized, and reflected light, using a Nikon Eclipse LV100 POL petrographic microscope equipped with a Nikon DS-Ri1 12-megapixel camera. The thick section was also examined in reflected light using the same microscope.

2.2. Scanning electron microscopy

Scanning electron microscopy (SEM) was carried out at the Zircon and Accessory Phase Laboratory (ZAPLab) at

Fig. 1. Northwest Africa (NWA) 7042 main mass. The exterior surface of the meteorite has a thin layer of desert varnish and a lighter coloured interior weathered zone. Dark veins of launch-generated melt are visible cross-cutting the sample face. Photo credit: Brian Boyle, Royal Ontario Museum.

the University of Western Ontario using a Hitachi SU6600 field emission scanning electron microscope (FE-SEM). The thin sections were carbon coated and energy dispersive X-ray spectroscopy (EDS) elemental x-ray intensity maps were collected using an Oxford Instruments X-Max 80 mm^2 silicon drift detector with a 15 kV electron beam. Color cathodoluminescence (CL) images were collected in four channels covering ultraviolet, visible, and near infrared spectra ranges with a Gatan ChromaCL detector system and Gatan Digital Micrograph software using a 10 kV electron beam. Cathodoluminescence imaging has become an important tool for identifying and visualizing the effects of shock metamorphism (i.e. Moser et al., 2013; Darling et al., 2016; Kayama et al., 2018) and is used here to analyze shock features in baddeleyite and maskelynite.

2.3. Electron Backscatter Diffraction (EBSD)

The sample was polished using a 50 nm alumina agent with a Buehler Vibromet II vibratory polisher to remove any nano-scale damage/deformation caused by previous polishing that would prevent diffraction, and then coated with a thin layer of carbon. Baddeleyite grains were located using a combination of automated backscatter electron (BSE) and EDS techniques using the ZAPLab's Hitachi SU6600 FE-SEM and Oxford Instruments INCA 'Feature' module. Grains were imaged using BSE and secondary electron techniques, and micro- to nano-scale structural analysis was conducted by EBSD using an Oxford Instruments Nordlys EBSD detector with a 20 kV electron beam with the sample tilted 70°. Generated baddeleyite diffraction patterns were matched to inorganic crystal structure database (ICSD) card 15,983 using crystal lattice parameters of $\alpha = 5.21$, $\beta = 5.26$, $\gamma = 5.37$, and $\alpha° = 90°$, $\beta° = 80.5°$, $\gamma° = 90°$ (Smith and Newkirk, 1965). Wild spike reduction was completed on all EBSD datasets, although no other form of raw data correction was conducted.

2.4. Micro-Raman spectroscopy

Micro-Raman spectra were collected in order to identify the high-pressure mineral phases in the shock veins and examine the altered olivine phases using a Horiba LabRAM ARAMIS micro-Raman spectrometer housed at the ROM. A 532 nm laser was used with the laser power filtered down to 2.1 mW to prevent sample damage. A 1200 groove/mm grating and 150 μm slit were used during collection. A Si reference material was used for calibration. Spectra were collected for 20 to 200 seconds at each point depending on the phase of interest. The RRUFF Raman database and CrystalSleuth (Laetsch and Downs, 2006; Lafuente et al., 2015) were used for mineral identification, followed by comparison with mineral literature data.

2.5. Electron Probe Microanalysis (EPMA)

Mineral compositions were acquired using the JEOL JXA-8230 electron microprobes at Queen's University and at the University of Toronto (sections were carbon-coated prior to mineral analysis). For analyses of olivine, pyroxene, oxides, and sulfides, accelerating potential was 15 kV, beam current was 20 nA, and the beam was fully focused. For analyses of maskelynite, glassy melt pockets, and phosphates, accelerating potential was 15 kV, beam current was 5 nA (maskelynite and melt) or 10 nA (phosphates), and the beam was defocused to a diameter of 10 microns. The XPP model of Pouchou and Pichoir (1991) as contained in the JEOL software (PC-EPMA version 1.9.2.0) was used to process the raw X-ray data. More detailed information on standards and diffracting crystals used can be found in the Supplemental Materials (Supplementary Table S1).

2.6. Transmission Electron Microscopy (TEM)

A TEM foil (~40 μm long) was prepared from the alteration area using a dual-beam SEM (Thermo Fisher Scientific Helios Nanolab 600i housed at the Environmental and Molecular Sciences Laboratory (EMSL) at Pacific Northwest National Laboratory) with focused ion beam (FIB) capabilities using conventional preparation FIB techniques (Giannuzzi and Stevie, 1999). A 30 kV accelerating voltage ion beam using progressively lower beam currents was used to extract and thin the lamella. A 2 kV accelerating voltage was used for the final cleaning/thinning step to remove surface beam damage. Two ~10 μm long "windows" (one closer to the core of the olivine, and one in the alteration margin) were thinned to <100 nm thickness.

Scanning TEM (STEM) analysis was performed with a probe-corrected FEI's Titan 80–300 operated at 300 kV to determine the particle morphology and crystallography. The STEM observations were performed using probe convergence angle of 18 mrad, and High Angle Annular Dark Field (HAADF) detector with inner collection angle three times higher than the probe convergence angle. TEM and diffraction observations were performed with Gatan's

UltraScan1000 2kx2k CCD camera. Compositional analysis was performed with EDS, using Oxford X-Max^{N}100TLE Solid Drift Detector (100 mm^2). The EDS data collection and processing was performed with Oxford's Aztec software package.

2.7. Bulk chemical analysis

Bulk rock major- and trace-element abundances were determined at the Scripps Isotope Geochemistry Laboratory (SIGL) and have been reported in Day et al. (2018). Digestion of 30–60 mg aliquots of NWA 7042 powder prepared from an interior whole-rock fragment were digested at 150 °C in Optima grade concentrated HF (4 mL) and HNO_3 (1 mL) for >72 hours on a hotplate, along with total procedural blanks and terrestrial basalt standards (Basalt Hawaiian Volcano Observatory (BHVO)-2, and Basalt Columbia River (BCR)-1 and BCR-2). Samples were sequentially dried and taken up in concentrated HNO_3 to remove fluorides, followed by dilution and doping with indium to monitor instrumental drift during analysis. Major- and trace-element abundance analyses were obtained using a ThermoScientific iCAP Qc quadrupole inductively coupled plasma mass spectrometer (Q-ICPMS) as described in Day et al. (2015). For major- and trace-elements, reproducibility of the reference materials was generally better than 6% (RSD).

3. RESULTS

3.1. Petrography and mineral chemistry

Northwest Africa 7042 consists of two generations of olivine (strongly-zoned early olivine Fo_{41-76}, and late-stage fayalitic olivine Fo_{46-56}), complexly zoned clinopyroxene, with interstitial optically isotropic plagioclase laths (maskelynite glass), accessory Mg-rich merrillite, apatite, pyrrhotite, ilmenite, spinels, and baddeleyite (Fig. 2, and Figs. S1-S2 in Supplementary Materials 1). Trace amounts of high-pressure mineral phases including ringwoodite, tuite, and symplectic breakdown products of the Mg-silicate perovskite were also identified within the shock veins that crosscut the primary igneous lithology. Both the igneous minerals and the launch-generated shock melt veins are in turn crosscut by terrestrial weathering veins predominantly consisting of calcite with traces of barite.

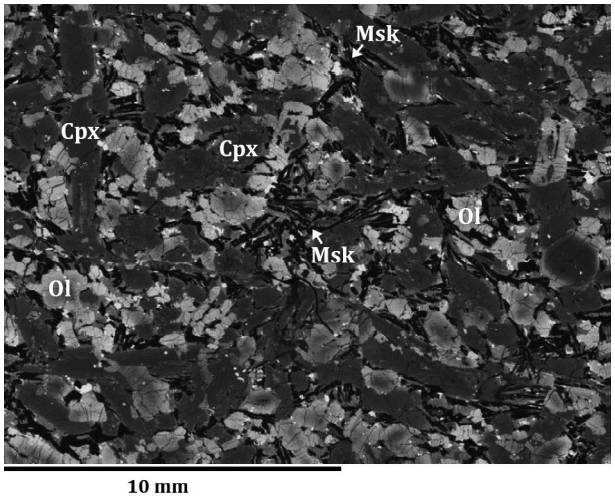

Fig. 2. Representative backscattered electron (BSE) image of NWA 7042 showing the macrocrystalline intergranular texture of the sample. Olivine grains (Ol) are light grey, clinopyroxene (Cpx) is medium grey, and intersertal maskelynite (Msk) laths are black.

The strongly zoned olivine crystals (0.15–1.6 mm) are blocky, subhedral, and contain conspicuous Mg-rich cores with a rusty orange-brown appearance in transmitted light (Fig. 3). Dark brown core margins ($Fo_{54.4-69.9}$; Table 1, Fig. 4) typically define the boundary between the orange-brown Mg-rich cores ($Fo_{60.8-76.1}$) and significantly less altered yellow–brown to colorless fayalitic rims ($Fo_{41.0-68.8}$). Some of the olivine cores have been amorphized by further alteration and appear dark brown in cross polarized light. The relatively sharp contacts between the darkened cores, core margins, and rims in the zoned olivine grains do not resemble the typical mottled heterogeneous textures associated with shock-darkened olivine (Takenouchi et al., 2018; discussed further in Section 4.1.1). Abundant micron-scale inclusions are also observed within most of the olivine cores, margins, and sometimes within the rims. Backscattered and transmission electron imaging of olivine reveals these inclusions correspond to small platelets of symplectic-textured intergrowths of chromite and a low-Mg, high-Ca silicate (Fig. 5). In one instance, a chromite inclusion is observed within a zone of ringwoodite associated with a crosscutting shock vein, demonstrating that the chromite-bearing inclusions predate the shock metamorphism (Fig. 5C). Ringwoodite lamellae are observed in both the fayalitic rims, and more forsteritic altered cores. Low EPMA totals <98.5% are consistently observed within the dark altered core margins, suggestive of the presence of water or voids within this phase (Table 1). Raman spectra collected within the altered olivine areas could not be used to identify any secondary alteration products due to fluorescence, with only weak olivine doublet peaks detected (Fig. S3 in Supplementary Materials 1).

On the thin section scale, several of the altered olivine grains are crosscut and displaced by shock veins. Terrestrial desert weathering veins of calcite and trace barite fill fractures that cut across the altered olivine cores and shock veins. While these terrestrial weathering veins are ubiquitous throughout the sample, they do not appear to have any correlation with the olivine alteration. A second generation of more Fe-rich zoned olivine grains with compositions ranging from $Fo_{45.9-55.8}$ are also observed. These grains are yellow–brown to colorless throughout (the same color as the Fe-rich rims of the forsteritic olivines), and do not contain dark cores.

TEM analysis of the altered core area reveals two distinct alteration textures including elongate dissolution voids, and Al-rich in-filled fractures or veins (Fig. 6). The dissolution voids are observed throughout the olivine core and core margin, are approximately 5–15 nm in width, and are all generally oriented parallel to the (001) plane of olivine. EDS analyses of these features shows depletion

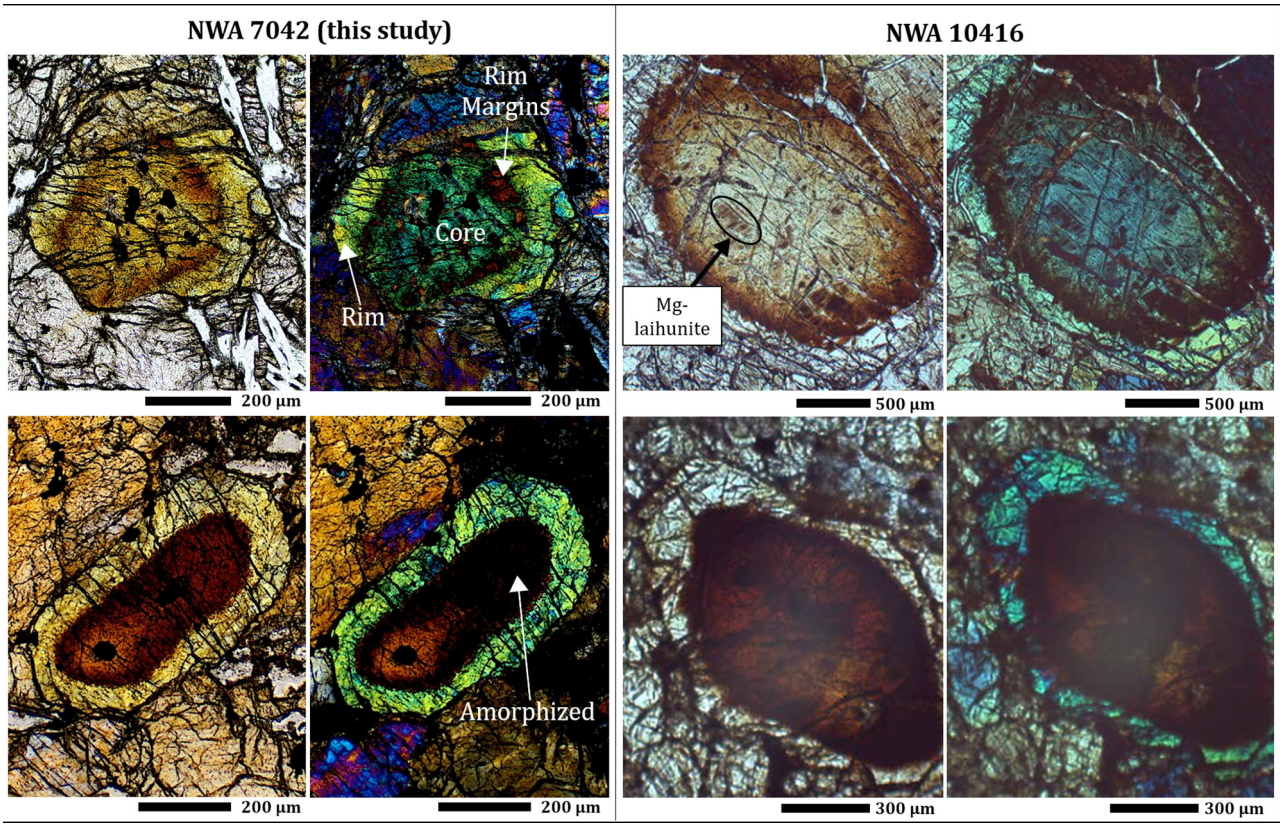

Fig. 3. Transmitted plane polarized light and cross polarized light images of altered olivine grains in NWA 7042 and NWA 10416. The Fe-rich rims in NWA 7042 are yellow in comparison with the colorless rims in NWA 10416. Secondary alteration product Mg-laihunite was also identified in NWA 10416 using micro X-ray diffraction and Raman spot analysis of NWA 10416 (after Vaci et al., 2020). (For interpretation of the references to colour in this figure legend, the reader is referred to the web version of this article.)

in all elements, and single-area electron diffraction (SAED) analyses show no evidence of crystallinity. The Al-rich fractures/veins are several microns long and up to 250 nm wide. SAED analyses only yields strong olivine diffraction patterns, and the Al-rich material was unable to be identified, although it is likely amorphous. In several instances, the fractures are cross-cut by the elongate dissolution features. The Al-rich features are in turn cross-cut and displaced by other thin fractures (Fig. 6C).

Pyroxene in NWA 7042 displays considerable compositional and textural variability. The most common occurrence is as elongate euhedral laths (typically 0.3–3.7 mm in length) with cores of Mg-rich and Ca-poor composition ($En_{53.0\text{-}64.3}Fs_{27.9\text{-}29.5}Wo_{5.1\text{-}14.6}$, FeO/MnO = 28.9–30.9) and Ca-rich, Mg-poor sub-calcic augite overgrowths ($En_{39.6\text{-}47.5}Fs_{22.0\text{-}27.0}Wo_{24.4\text{-}33.9}$, FeO/MnO = 28.5–31.1). These pyroxene grains form an intersertal texture with splays of maskelynitized feldspar within the interstices. Additional Fe-rich pyroxene (compositionally ferropigeonite; $En_{34.8\text{-}44.9}Fs_{38.5\text{-}46.1}Wo_{9.6\text{-}18.7}$, FeO/MnO = 31.4–37.3; and varying from approximately 20–400 µm in length) occurs intergrown with the maskelynite laths, and is associated with merrillite, oxides and pyrrhotite. All three of the pyroxene occurrences, namely Mg-rich cores, calcic rims, and ferropigeonite intergrown with maskelynite, are devoid of exsolution lamellae.

Maskelynite ($An_{38.9\text{-}53.9}Ab_{43.6\text{-}61.3}Or_{1.9\text{-}5.3}$) occurs as splays of lath-like grains (varying from 0.03-1.4 mm in length) commonly in roughly parallel intergrowths with the larger pyroxene laths. CL imagery of maskelynite (Fig. S4 in Supplementary Materials 1) reveals the common presence of sector zoning, which is also visible in high-contrast backscatter imagery. CL activity is greater in zones with lower BSE signal. Ferropigeonite, merrillite, oxides, and pyrrhotite are observed within the interstices between the (former) plagioclase laths. The maskelynite is free of vesicles and predominantly appears to retain the shape of the pre-shocked plagioclase. Local patches of mesostasis are also commonly observed associated with maskelynite; these are rich in Si and K, and poor in Al, and contain submicron quench crystallites (Fig. 7).

Merrillite is the most common phosphate mineral observed in NWA 7042. Apatite is typically observed rimming merrillite in contact with maskelynite. EPMA of apatite shows that they contain approximately equal concentrations of F and Cl on an atomic basis. NWA 7042 merrillite is low in Na compared to most martian merrillite analyses (Shearer et al., 2015), reflecting the role of plagioclase crystallization prior to merrillite.

Oxide minerals (including ilmenite, and the spinel phases chromite, ferrichromite, and titanomagnetite) most commonly occur in association with maskelynite, ferropi-

Table 1
Representative mineral compositions of major and minor phases in NWA 7042.

	Altered Olivine			Groundmass Olivine		Ringwoodite	Pyroxene			Maskelynite	Coarse-Grained Mesostasis	Fine-Grained Mesostasis	Merrillite	Apatite	Tuite	Spinels	Ilmenite	Pyrrhotite
	Cores	Rim Margins [2]	Rims	Cores	Rims		Cores	Rims	Ferropigeonite									
	(n = 38)	(n = 21)	(n = 44)	(n = 3)	(n = 4)	(n = 3)	(n = 8)	(n = 7)	(n = 9)	(n = 15)	(n = 3)	(n = 5)	(n = 20)	(n = 4)	(n = 3)	(n = 13)	(n = 10)	(n = 20)
Oxide wt %																		
SiO_2	37.3	35.9	35.4	34.7	34.3	20.6	53.2	51.2	49.7	55.7	61.1	78.6	0.29	0.65	0.81	0.03	0.05	–
P_2O_5	0.10	0.09	0.08	0.12	0.08	0.16	–	–	–	0.07	0.01	0.10	45.5	41.6	45.2	–	–	–
Al_2O_3	0.30	0.54	0.19	0.11	0.21	2.89	0.73	1.84	1.06	26.5	22.9	12.1	0.07	0.11	0.14	3.87	0.08	–
TiO_2	0.05	0.07	0.07	0.04	0.08	0.08	0.15	0.41	0.67	0.07	0.07	0.24	0.01	0.02	0.03	14.0	51.1	–
Cr_2O_3	0.04	0.07	0.04	0.01	0.02	0.11	0.49	0.64	0.08	0.02	0.01	0.01	0.01	0.00	0.01	20.0	0.27	–
V_2O_3	0.01	0.02	0.01	0.01	<0.01	0.02	0.05	0.09	0.04	–	–	–	–	–	–	0.49	0.18	–
SO_3	–	–	–	–	–	–	–	–	–	–	–	–	–	–	–	–	–	38.60
FeO	26.3	31.1	36.5	39.4	41.6	50.6	18.3	15.1	26.2	0.78	0.54	0.42	1.80	0.76	2.84	41.3	40.7	60.80
Fe_2O_3	–	–	–	–	–		–	–	–	–	–	–				17.4	4.07	–
MnO	0.50	0.53	0.67	0.71	0.76	0.28	0.61	0.51	0.76	0.03	0.00	0.01	0.10	0.11	0.12	0.57	0.71	–
MgO	34.1	29.1	26.5	24.5	22.2	9.8	22.2	15.3	14.0	0.08	0.02	0.02	2.92	0.18	2.83	1.96	2.46	–
NiO	0.07	0.06	0.04	0.04	0.04	0.06	0.03	0.01	0.02	–	–	–	–	–	–	0.03	0.01	0.55
CaO	0.30	0.40	0.26	0.23	0.24	2.32	3.96	14.0	6.4	9.9	5.9	2.80	47.2	52.8	47.1	0.09	0.17	–
Na_2O	0.01	0.01	0.01	0.01	0.01	0.15	0.05	0.17	0.07	5.6	6.4	3.54	1.14	0.20	1.20	–	–	–
K_2O	0.01	0.02	0.01	<0.01	0.03	0.35	0.01	0.01	0.01	0.56	2.21	1.68	0.04	0.02	0.03	–	–	–
Nb_2O_5	–	–	–	–	–	–	–	–	–	–	–	–	–	–	–	0.00	0.01	–
SrO	–	–	–	–	–	–	–	–	–	–	–	–	0.02	0.01	0.01	–	–	–
Y_2O_3	–	–	–	–	–	–	–	–	–	–	–	–	0.07	0.01	0.10	–	–	–
F	–	–	–	–	–	–	–	–	–	0.04	0.09	0.10	bdl	1.23	bdl	–	–	–
Cl	–	–	–	–	–	–	–	–	–	0.01	0.01	0.00	bdl	2.27	bdl	–	–	–
Total	99.1	97.8 [8]	99.8	99.9	99.6	87.5 [9]	99.8	99.3	99.1	99.3	99.4	99.7	99.3	100.0	100.5	99.7	99.7	100.0
Olivine																		
Fo	69.7	59.6	56.3	52.6	48.7													
Σ Oct Site	2.00	1.98	1.99	2.00	2.01													
Σ Tet Site	1.00	1.00	1.00	1.00	0.99													
Pyroxene																		
En							62.9	45.2	42.0									
Fs							29.1	25.1	44.1									
Wo							8.1	29.7	13.9									
Feldspar																		
An										48.0								
Ab										48.7								
Or										3.2								

Notes:
1) n = number of points analysed.
2) Alteration Rims refers to the dark brown alteration area around the olivine cores (in between the Mg-rich cores, and less altered Fe-rich rims).
3) Fo = Forsterite number (atomic $Mg^{2+}/(Fe^{2+}+Mg^{2+})$).
4) Oct = Octahedral site in olivine (sum of Al, Ti, V, Cr, Fe, Mn, Mg, Ca, Na, K, and Ni atoms per formula unit).
5) Tet = Tetrahedral site in olivine (sum of Si, and P atoms per formula unit).
6) En = Enstatite (atomic $Mg^{2+}/(Mg^{2+}+Ca^{2+}+Fe^{2+})$), Wo = Wollastonite (atomic $Ca^{2+}/(Mg^{2+}+Ca^{2+}+Fe^{2+})$), Fs = Ferrosillite (atomic $Fe^{2+}/(Mg^{2+}+Ca^{2+}+Fe^{2+})$).
7) An = Anorthite (atomic $Ca^{2+}/(K^{+}+Na^{+}+Ca^{2+})$), Ab = Albite (atomic $Na^{2+}/(K^{+}+Na^{+}+Ca^{2+})$), Or = Orthoclase (atomic $K^{+}/(K^{+}+Na^{+}+Ca^{2+})$).
8) bdl = below detection limit.
9) "–" = not determined.
10) Low totals for the dark alteration core margins are possibly due to the presence of water or voids.
11) Low totals for the ringwoodite is possibly due to mixing with other phases (likely oxides).

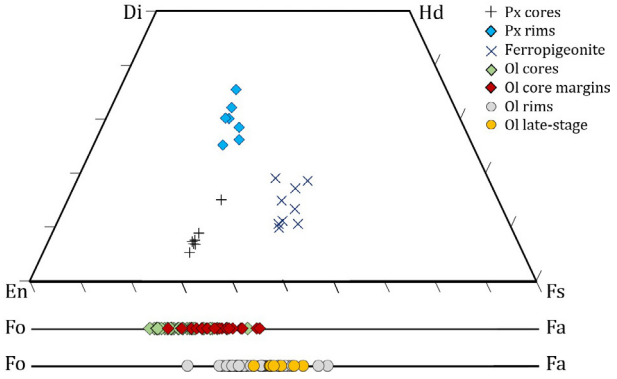

Fig. 4. Olivine and pyroxene mineral compositions in NWA 7042. Px = pyroxene, Ol = olivine. Late-stage (see yellow circles) refers to the second generation of more Fe-rich olivine that do not contain altered cores. (For interpretation of the references to colour in this figure legend, the reader is referred to the web version of this article.)

geonite, and merrillite. Magnesian-rich, Ti-poor chromite is commonly observed partially enclosed within olivine. Sulfides are chemically homogeneous, with minor Ni, Cu and Co, and compositions close to Fe_9S_{10} consistent with pyrrhotite. Trace baddeleyite in NWA 7042 is commonly associated with late-stage crystallization assemblages located throughout the sample.

3.2. Shock features

Evidence of high pressure and temperature shock metamorphism in NWA 7042 includes the presence of maskelynite, pervasive fracturing of olivine and pyroxene, planar fractures in olivine, the formation of melt veins, displacement along shock veins, and the presence of high-pressure mineral phases including the symplectic breakdown products of Mg-silicate perovskite, ringwoodite, and tuite. To better constrain the shock pressures and temperatures experienced by NWA 7042, CL and EBSD analyses of baddeleyite grains were also completed.

3.2.1. Shock veins and high-pressure minerals

Northwest Africa 7042 contains several melt-rich veins which crosscut primary igneous minerals (Fig. 7) sometimes resulting in the formation of reaction rims. Lamellar growths of ringwoodite are observed extending into both the unaltered fayalitic olivine rims and altered olivine cores when in contact with shock veins (identified using BSE imaging, and Raman micro-spectroscopy; Fig. 8) Similar ringwoodite lamellae have been reported from shock melt veins in other shergottites and Raman spectra of the phase have consistent diagnostic peaks occurring at ~790 cm^{-1} and ~842 cm^{-1} (Fig. 8; Baziotis et al., 2013; Walton et al., 2014).

The shock veins (ranging from 20–200 μm in diameter) are slightly curved and mainly comprise partially crystallized melt material. These veins are not observed to originate from or connect between melt pockets, and do not contain vesicles. The shock veins also contain several high pressure mineral phases including an oxide-silicate mixture consistent with the breakdown of bridgmanite (perovskite-structured $(Mg,Fe)SiO_3$; Tschauner et al., 2014) into a symplectic intergrowth consisting of Mg-silicate glass and nanoscopic grains of an Fe-rich oxide that is likely magnesiowüstite (Figs. 7 & 8). Raman spectroscopy of these symplectic grains shows evidence of vitrified perovskite, similar to that documented in shock veins of the Tissint meteorite

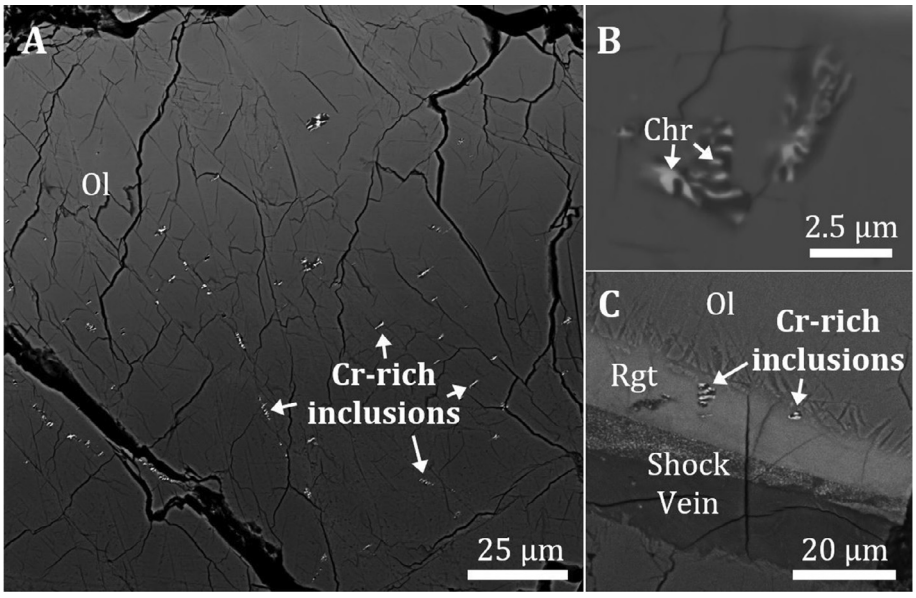

Fig. 5. Scanning electron microscope (SEM)-BSE images of symplectite chromite-silicate growths within NWA 7042 olivine; (A) Typical distribution of the Cr-rich inclusions in olivine (Ol). Note that the inclusions are not observed within the rim; (B) Higher magnification view of the symplectite-like texture in the Cr-rich inclusions (Chr = chromite); (C) Cr-rich inclusions within ringwoodite (Rgt), demonstrating that they are unaffected by the phase transformation.

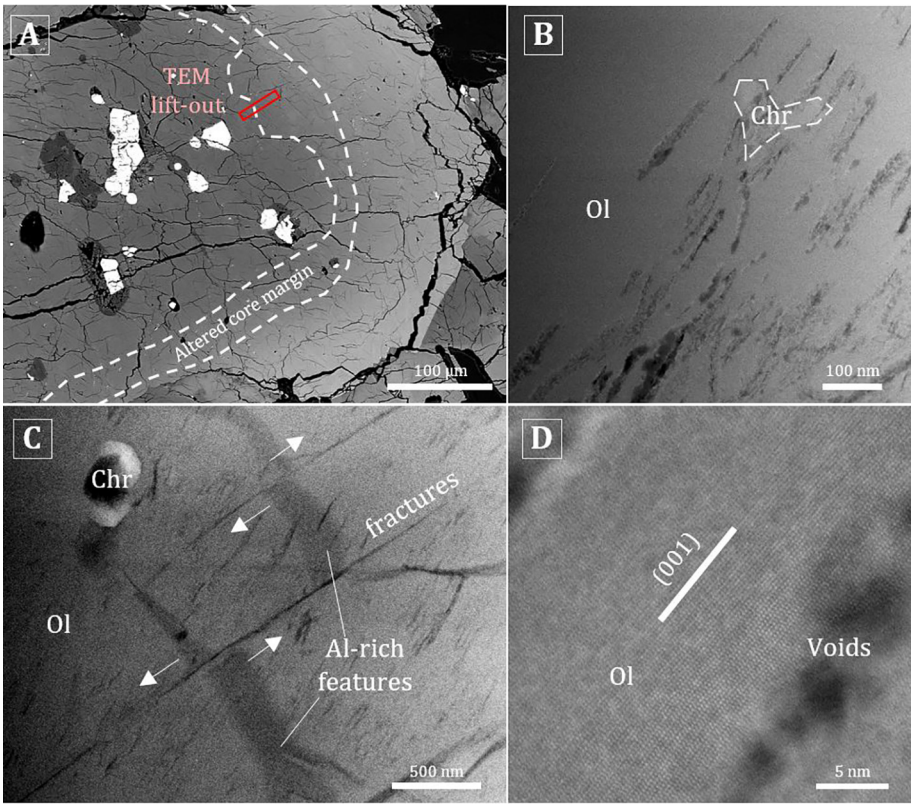

Fig. 6. (A) BSE image of the TEM lift-out area within the altered olivine (Ol) core. (B) STEM image of semi-aligned dissolution texture with a ~150 nm chromite (Chr) grain in the olivine core. (C) STEM image of the thick Al-rich features and dissolution texture. The white arrows denote the apparent offset of the Al-rich features by fractures. (D) STEM image of the dissolution texture, showing no crystallinity within the black voids, and the direction of the (001) olivine plane for reference.

(Baziotis et al., 2013; Walton et al., 2014). Raman spectra of shock vein phosphates (Fig. 8) match that of tuite (γ-$Ca_3(PO_4)_2$) with a primary diagnostic peak located at ~974 cm^{-1} (e.g. Baziotis et al., 2013). Tuite has been reported from shock veins of the Suizhou L6 chondrite (Xie et al., 2003) and in synthesis experiments using both natural apatite (Xie et al., 2013) and stoichiometric mixtures of $CaHPO_4$ and $CaCO_3$ (Zhai et al., 2010). Tuite has been documented in several martian meteorites including Tissint (Baziotis et al., 2013) and Chassigny (Fritz and Greshake, 2009). The identified high-pressure phases in NWA 7042 are observed exclusively within, or in contact with, the shock veins.

3.2.2. Shock features in baddeleyite

Baddeleyite in NWA 7042 is commonly associated with Fe-Ti oxides (ilmenite and titanomagnetite) and Fe-sulfides (pyrrhotite), in late-stage crystallization assemblages located throughout the sample (Fig. S9 in Supplementary Materials 1). Despite appearing smooth and homogenous in BSE imaging, the baddeleyite display an abundance of microstructural features in CL and EBSD analysis. Most notably, mottled and oscillatory textures in CL and poorly diffracting (quasi-amorphous) grains highlight the shocked nature of the population (Fig. S10 in Supplementary Materials 1). Taken in concert, these features place the grains in shock group 2 as defined by Darling et al. 2016, suggesting that U-Pb analysis of the grains would yield partially reset ages that do not correlate with a crystallization or impact event. The highly shocked nature of the grains is further supported by the deformed nature of the surrounding pigeonite, which exhibit up to 35° of crystal plastic deformation.

3.3. Bulk composition

The bulk rock REE pattern is similar to other intermediate shergottites, with La/Yb_N values of 0.41 and 0.40 (Table 2, Fig. 9). The bulk rock Mg# is 57.9 for both replicates. A slight positive Eu anomaly is observed in both replicates, which does not appear to be common in other intermediate shergottites. The source of the Eu anomaly would be consistent with minor plagioclase accumulation, although feldspar (maskelynite) makes up approximately 9 modal%, within the normal range for shergottites. Depleted martian meteorite Dar Al Gani (DaG) 476 also appears to have a slight anomalous Eu concentration (Fig. 9; Day et al., 2018). This sample is known to have experienced significant terrestrial weathering (Crozaz and Wadhwa, 2001). Europium anomalies have also been detected within the alteration phases of nakhlite NWA 817, interpreted to be from the fluid that altered the olivine

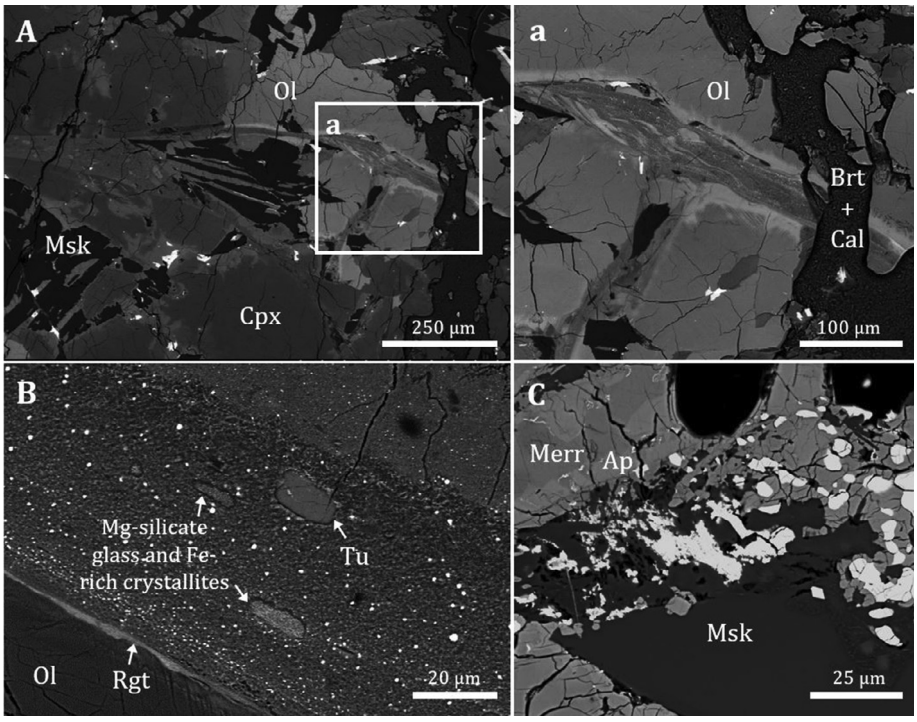

Fig. 7. Representative BSE images of shock and late-stage crystallization features in NWA 7042. (A) Launch-generated shock vein cross-cutting olivine (Ol) and clinopyroxene (Cpx). Flow textures within the vein are magnified in inset (a) and are cross-cut by a terrestrial weathering vein comprised of calcite (Cal), and minor barite (Brt). (B) Launch-generated shock-vein that has entrained surrounding minerals and contains high-pressure mineral phases, including tuite (Tu) and ringwoodite (Rgt) at the contact between the shock vein and olivine. (C) Typical mesostasis pocket associated with maskelynite consisting of late-stage crystallization phases including merrillite (Merr), and apatite (Ap). The mesostasis pockets are highly heterogeneous and contain abundant submicron crystallites, likely including silicate, oxide, and possibly sulfides.

on Mars (Gillet et al., 2001). At this time, the phase that is the source of excess Eu in NWA 7042 is not constrained.

4. DISCUSSION

4.1. Olivine modification

The chemical analysis of aqueous alteration products in martian meteorites can provide new insights into the chemistry of water reservoirs, the conditions under which these rocks were once altered, and possibly even the timing of that alteration. As such, determining the origin of alteration products (specifically if they are martian or terrestrial) within meteorite finds like NWA 7042 is particularly valuable. As brown olivine in martian meteorites is also known to be caused by "shock-darkening" (e.g. Takenouchi et al., 2018), this process must also be considered. Here, we summarize our preliminary geochemical and petrographic analysis of altered olivine in NWA 7042 and examine the possibility of martian, terrestrial, and shock-darkening formation mechanisms.

4.1.1. Shock-darkening

Shock-darkened olivine has been observed in a wide variety of martian meteorites, and is associated with relatively high pressure and temperature impact events (~55 GPa, and >1200–1170 K; Takenouchi et al., 2018). This type of olivine appears dark-brown in transmitted light due to the presence of small amounts of Fe^{3+} (from the oxidation of Fe^{2+} during a shock event; Ostertag et al., 1984) and/or the presence of nano-scale inclusions of Fe metal (Treiman et al., 2007).

The brown olivine observed in NWA 7042 does not resemble typical shock-darkening which occurs as dark-brown irregular patchy or mottled zones in olivine and does not have the rusty red-brown color observed in NWA 7042 (Takenouchi et al., 2018). Moreover, TEM analysis of the olivine cores in NWA 7042 also did not reveal any of the Fe-metal inclusions usually associated with shock-darkened olivine in other martian meteorites (Treiman et al., 2007). The presence of brown olivine within the Mg-rich cores of NWA 7042 is also not typical of shock-darkening, as it is not known to correspond to compositional variations (Takenouchi et al., 2018) although there are rare exceptions. In shergottite Larkman Nunatak (LAR) 06319, shock-darkened olivine is more commonly observed in the Fe-rich rims of zoned olivine; opposite to the brown olivine zonation observed in NWA 7042 (Takenouchi et al., 2018). Reverse "darkening" (where olivine cores are darker than rims) has been observed in a few olivine grains within poikilitic shergottite Lewis Cliff (LEW) 88516, but is not nearly as pervasive and occurs in irregular/patchy zones that do not correlate with compositional zoning (Takenouchi et al., 2018). The lack of nano-

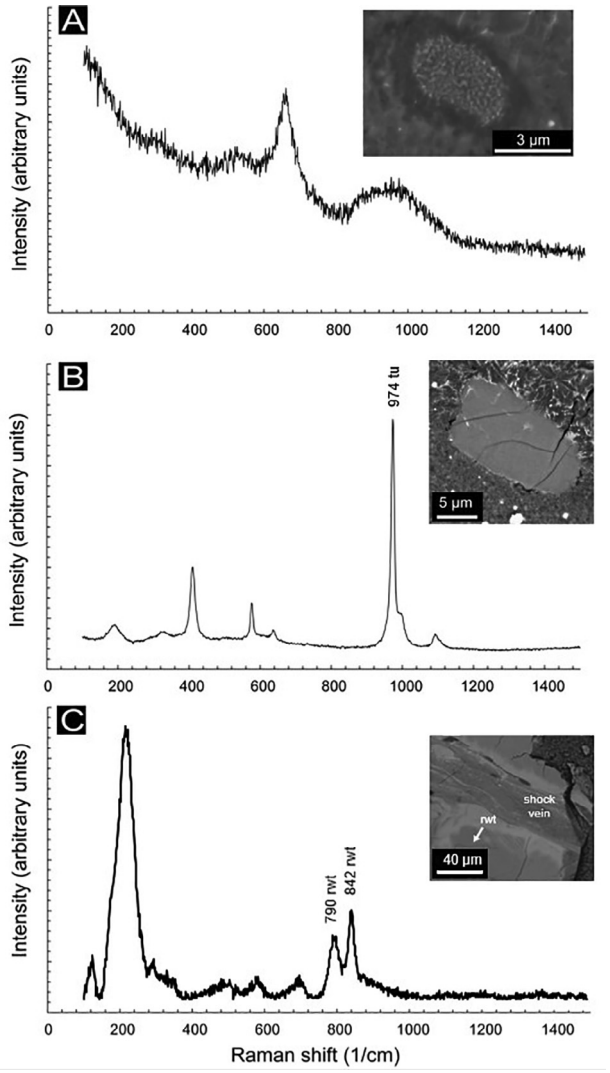

Fig. 8. Representative Raman spectra and SEM-BSE images of high-pressure materials within NWA 7042 shock veins. (A) Symplectic intergrowth of magnesiowüstite and vitrified Mg-silicate perovskite; (B) Tuite, and (C) Contact between shock melt vein and olivine with lamellar ringwoodite (rgt), with characteristic Raman peaks marked.

scale metal inclusions, and the presence of brown olivine only within the Mg-rich cores in NWA 7042 make shock-darkening an unlikely formation mechanism.

4.1.2. Alteration on Mars

The altered olivine cores in NWA 7042 do not resemble typical secondary alteration products previously observed in martian meteorites. The most common alteration phase of martian origin, "iddingsite," typically occurs along mineral grain boundaries or fractures as alteration veinlets that crosscut olivine and pyroxene (Treiman et al., 1993; Lee et al., 2015). It should be noted that the term "iddingsite" has a variety of definitions. Within the nakhlites it is used to describe veins or veinlets comprising poorly crystalline, fine-grained mixtures of secondary alteration products including hydrous silicates, sulphates, carbonates, halides, and oxides deposited during hydrothermal events at or near the surface of Mars (Lee et al., 2015). However, the original definition of "iddingsite" is an alteration product that forms via sub-solidus magmatic alteration of olivine before the rock has fully crystallized (i.e. deuteric alteration by residual melts and fluids; Ross and Shannon, 1925; Edwards, 1938; Delvigne et al., 1979; Kuebler, 2013; Vaci et al., 2020). The presence of pristine olivine rims around the altered cores in NWA 7042 indicates that the alteration occurred prior to the crystallization of the un-altered rims, and therefore most likely took place within the host magma itself. Several of the olivine cores are also crosscut and displaced by shock veins, indicating that the alteration may have occurred prior to the shock event that ejected it from Mars (Fig. 10). As such, here we examine the possibility that the olivine cores were altered deuterically on Mars, and contrast this to the similarly altered shergottite NWA 10416 and several terrestrial basalts and gabbros.

In terrestrial settings, deuterically altered olivine has been observed in many different localities including: the Cantal volcano lava plateaus (France), basalt flows, gabbros, and pegmatoids in French Polynesia (Bora Bora, Maupiti, Eiao, Ua Huka, Marquesas archipelago, Huahine, and Moorea), basaltic andesites in San Ignacio, Baja California (Mexico), potassic lava flows from Singu (Myanmar), Sukadana (Sumatra), basaltic andesite flows from Cerro Picacho (Chile), the Victorian basalts (Australia), basalts from Banat (Romania), Hinsdale volcanic series basalts (New Mexico, USA), Panorama Point basalt (Oregon, USA), and the Los Magotes and La Jara Creek basalts (Colorado, USA) (Ross and Shannon, 1925; Edwards, 1938; Goff, 1996; Caroff et al., 2000; Clément et al., 2007; Tschegg et al., 2010; Vaci et al., 2020). These terrestrial examples are highlighted here as they contain altered olivine grains that are optically and chemically similar to the olivine in NWA 7042 and shergottite NWA 10416 with dark brown deuterically altered cores and pristine olivine rims (Fig. 11; Ross and Shannon, 1925; Edwards, 1938; Goff, 1996; Caroff et al., 2000; Clément et al., 2007; Tschegg et al., 2010; Vaci et al., 2020). The terrestrial samples noted here were collected at depth and are typically reported as fresh and devoid of weathering (Ross and Shannon, 1925; Edwards, 1938; Goff, 1996; Caroff et al., 2000; Clément et al., 2007; Tschegg et al., 2010; Vaci et al., 2020).

The alteration products produced during deuteric alteration of olivine in terrestrial samples are generally referred to as high temperature iddingsite (HTI) because of their optical similarities with low-temperature post-magmatic iddingsite (LTI) (Goff, 1996; Caroff et al., 2000; Clément et al., 2007). High temperature iddingsite forms via alteration of olivine at temperatures higher than 1075 °C in mafic magmas with unusually high water contents and high oxygen fugacity (above the Nickel-Nickel-Oxide (NNO) buffer; Clément et al., 2007). The composition of HTI in terrestrial samples has been determined by X-ray diffraction and consists of cryptocrystalline aggregates of orthopyroxene, cristoballite, amorphous silica, maghemite, hematite, and magnetite, and is also characterized by a deficit in EPMA totals, interpreted as the result of water incorpora-

Table 2
NWA 7042 whole-rock major and trace element abundances.

	Sample		Terrestrial Standards			
	NWA 7042	NWA 7042 rpt	BHVO-2	RSD	BCR-2	RSD
SiO_2	40.6	44.9	50.56	1.4%	53.44	2.1%
TiO_2	0.81	0.74	2.73	1.1%	2.34	3.0%
Al_2O_3	4.83	4.25	13.50	2.2%	13.85	4.4%
Fe_2O_3T	24.0	22.4	11.40	0.7%	13.51	1.7%
MgO	18.5	17.3	7.23	1.0%	3.90	4.4%
MnO	0.55	0.51	0.17	0.9%	0.20	3.1%
CaO	8.99	8.38	11.40	0.9%	7.32	4.3%
Na_2O	0.80	0.64	2.22	7.1%	3.18	8.2%
K_2O	0.05	0.08	0.52	2.5%	1.87	6.3%
P_2O_5	0.94	0.85	0.27	1.2%	0.38	4.2%
Sum	100	100	100	–	100	–
Mg#	57.9	57.9	53.1	0.3%	34.0	3.3%
Li	5.57	5.90	4.8	1.5%	10.09	6.2%
B	11.66	14.24	2.4	6.4%	4.18	6.5%
Sc	36.44	37.69	32.0	1.3%	34.08	6.2%
V	227	231	317.0	1.4%	421.29	6.4%
Cr	4383	4381	280.0	1.4%	18.48	6.8%
Co	61.53	63.63	45.0	1.4%	38.50	6.4%
Ni	207.89	212.31	119.0	1.3%	12.20	5.1%
Cu	10.74	10.64	127.0	1.1%	19.83	5.6%
Zn	72.19	75.80	103.0	1.2%	156.86	6.9%
Ga	13.56	14.04	22.0	0.9%	23.08	6.7%
Ge	2.04	2.03	1.6	1.9%	1.77	6.0%
Se	0.12	0.06	0.10	5.0%	0.12	12.5%
Rb	1.02	1.05	9.1	0.6%	47.10	6.4%
Sr	75.41	76.49	396.0	1.3%	346.72	6.0%
Y	13.26	13.55	26.0	1.1%	36.27	5.1%
Zr	36.70	37.94	172.0	1.6%	189.77	5.9%
Nb	1.19	1.25	18.1	0.9%	12.45	5.5%
Mo	0.11	0.16	4.0	19.8%	259.40	11.9%
Cs	0.05	0.04	0.10	3.2%	1.11	4.9%
Ba	289.25	320.47	131.0	5.4%	678.14	6.0%
La	0.70	0.71	15.2	1.7%	24.95	5.4%
Ce	1.76	1.80	37.5	1.8%	52.87	5.2%
Pr	0.28	0.29	5.4	2.0%	6.90	5.1%
Nd	1.60	1.71	24.5	2.1%	28.88	5.1%
Sm	0.97	1.00	6.1	1.7%	6.52	5.5%
Eu	0.53	0.55	2.1	1.9%	2.11	6.1%
Gd	1.71	1.82	6.2	1.0%	6.99	6.9%
Tb	0.35	0.38	0.9	1.8%	1.05	5.6%
Dy	2.48	2.57	5.3	1.6%	6.37	6.0%
Ho	0.51	0.52	1.0	2.9%	1.29	5.5%
Er	1.38	1.42	2.5	2.7%	3.65	5.5%
Tm	0.20	0.20	0.3	2.3%	0.52	6.2%
Yb	1.20	1.18	2.0	2.3%	3.34	5.8%
Lu	0.17	0.17	0.3	2.6%	0.49	4.5%
Hf	1.27	1.26	4.4	2.7%	4.87	4.3%
Ta	0.06	0.06	1.1	2.5%	0.76	5.1%
W	0.12	0.12	0.2	4.1%	0.44	6.0%
Pb	0.32	0.40	1.6	6.0%	10.93	4.9%
Th	0.12	0.12	1.2	3.6%	5.95	4.8%
U	0.09	0.09	0.4	4.4%	1.60	4.7%

Notes:
1) BHVO = Basalt, Hawaiian Volcano Observatory (terrestrial standard).
2) BCR = Basalt, Columbia River (terrestrial standard).
3) RSD = Relative Standard Deviation.

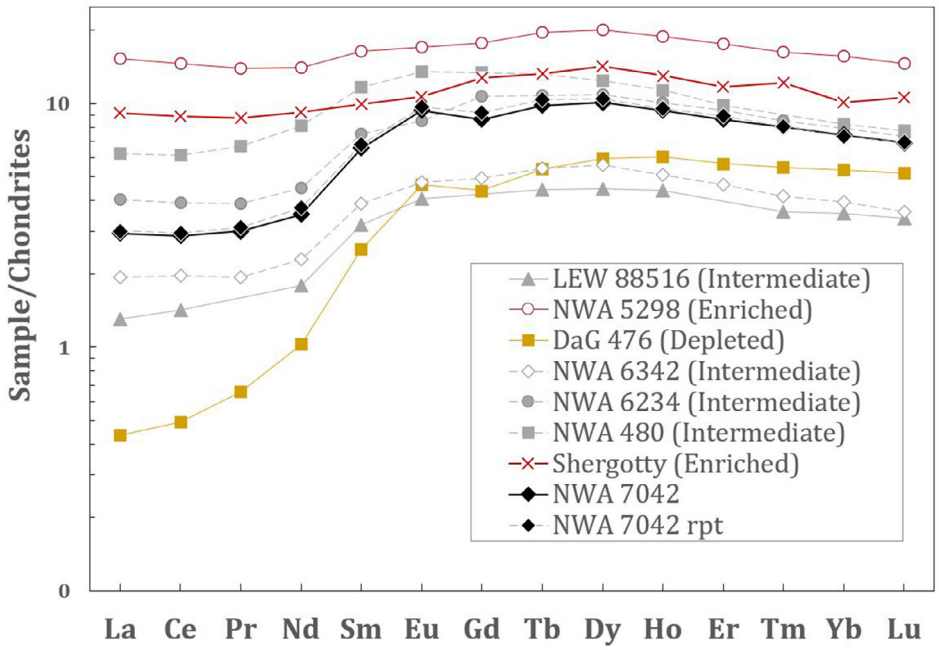

Fig. 9. CI-chondrite-normalized rare earth element (REE) diagram comparing enriched (En), intermediate (Int), and depleted (Dep) shergottites to the bulk analysis of NWA 7042 and replicate (NWA 7042-rpt) from Day et al., 2018. The REE abundances in each sample have been normalized over REE abundances in CI chondrites (McDonough and Sun, 1995). Sources for bulk chemical data: NWA 7042 (Day et al., 2018), NWA 480 (Barrat et al., 2002), NWA 6234 (Filiberto et al., 2012), NWA 6342 (Day et al., 2018), LEW 88516 (Dreibus et al., 1992), Shergotty (Lodders, 1998), NWA 5298 (Day et al., 2018), Dar al Gani 476 (Day et al., 2018).

tion (Goff, 1996; Clément et al., 2007). Clément et al. (2007) also determined that a significant portion of Fe in olivine is oxidized within these HTI zones, pointing to the formation of the high temperature alteration phase laihunite ($Fe^{3+}[Mg^{2+},Fe^{2+}]_{0.5}\square_{0.5}[SiO_4]$) along with maghemite and magnetite. Experimental studies have shown that laihunite occurs along with magnesioferrite via oxidation of fayalitic olivine at temperatures above 600 °C, and has been identified in several nakhlites, and within the cores of similarly altered olivine in NWA 10416 (Noguchi et al., 2009; Vaci et al., 2020). Previous TEM analyses on deuterically altered terrestrial olivine from basaltic andesites (Oregon, USA) reveal high-temperature oxidation assemblages of magnetite plus silica, and olivine-laihunite intergrowths oriented parallel to olivine's (001) plane (Banfield et al., 1990). TEM analysis of deuterically altered olivine from La Jara Creek basalt (Colorado, USA) shows the alteration mainly consists of discontinuous lineations of amorphous material (~10–20 nm wide) and pore space, with no laihunite or magnetite plus silica assemblages identified (Vaci et al., 2020). Similar textures are also observed from TEM foils collected in the altered olivine cores in NWA 10416 (Vaci et al., 2020; Piercy et al., 2020). In this case, Mg-laihunite was still identified in the olivine grains within NWA 10416 using μXRD, likely because the XRD analyses were sampling a much larger area and the TEM foils may have not been collected in laihunite-rich areas (Vaci et al., 2020). The high-temperature phases noted here were not observed in our preliminary TEM analysis of NWA 7042, although the discontinuous dissolution voids closely resemble the textures observed within the deuterically altered olivine cores of the La Jara Creek basalt (Vaci et al., 2020). The dissolution voids in NWA 7042 cross-cut both the Al-rich alteration filled fractures/veins and some of the nano-scale chromite inclusions meaning that at least one generation of dissolution must have occurred after chromite crystallized and after the deposition of the Al-rich alteration product. The Al-rich veins are in turn crosscut and displaced by fractures (Fig. 6) complicating this interpretation further.

The boundary between the altered cores and the olivine rims in deuterically altered martian and terrestrial samples points to a two-step crystallization process with a sudden termination of the alteration reaction, and a reversal to olivine precipitation (Edwards, 1938; Goff, 1996; Caroff et al., 1997; Caroff et al., 2000; Clément et al., 2007). In terrestrial basalts and gabbros, the altered cores are thought to have formed through interaction of olivine and volatile-rich residual melt as the magma was being emplaced, but before the rock fully crystallized on or closer to the surface (Edwards, 1938; Goff, 1996; Caroff et al., 1997; Caroff et al., 2000; Clément et al., 2007). This alteration process occurs due to a temporary increase in oxygen fugacity (fO_2) in the residual melt (Goff, 1996; Caroff et al., 1997; Caroff et al., 2000; Clément et al., 2007). The temporary increase in fO_2 is ascribed to an increase of H_2O in the residual melt; sourced from either late-stage incorporation of meteoric water (Goff, 1996), or magmatic water from the origin that is excluded from early growing crystals (Caroff et al., 1997; Caroff et al., 2000; Clément et al., 2007). During ascent and pressure decrease, volatiles within the residual melt will begin to degas with the dissolved

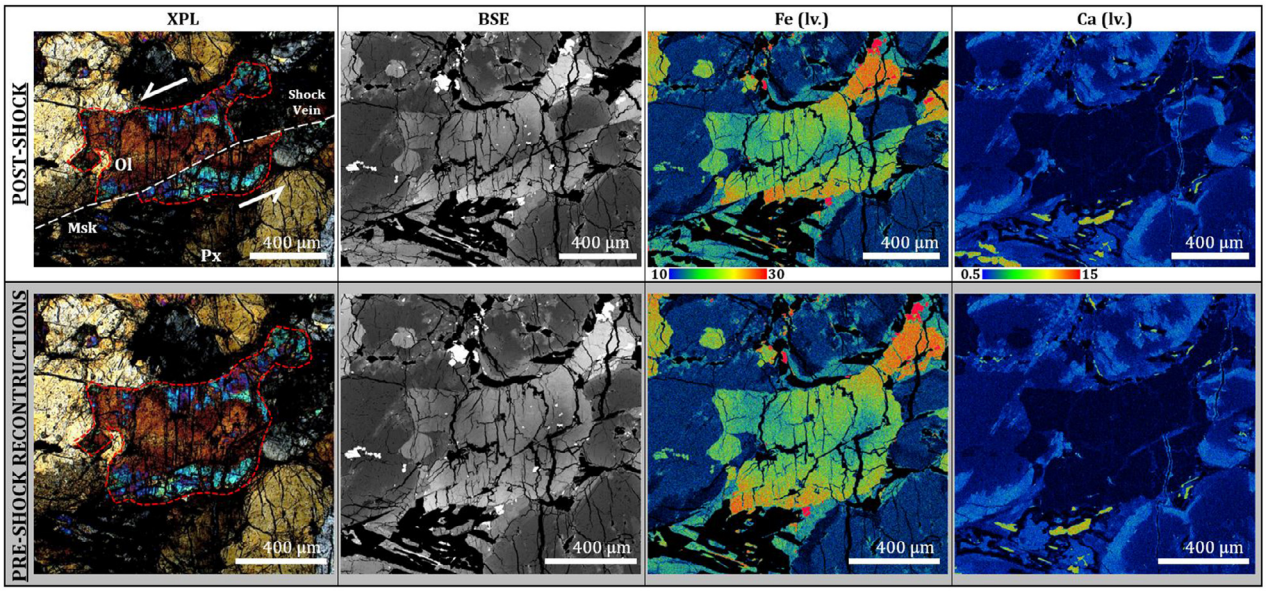

Fig. 10. Cross-polarized light (XPL), backscattered electron (BSE), and wavelength dispersive spectroscopy (WDS) maps of Fe and Ca concentrations of an altered olivine in NWA 7042 that has been crosscut and displaced by a shock vein. Reconstructions of how the olivine grain may have been situated prior to the shock event are provided in the bottom panel. After reconstruction, the dark margin of the altered core in XPL, brightness levels in BSE, and Fe concentrations all line up indicating that the original geochemical signature (prior to the shock event) is preserved. It should be noted that the exact vector of displacement is unknown, and extremely unlikely to be two-dimensional. Any discrepancies across the shock vein may be due to displacement along the third dimension in or out of the plane of the sample. The Ca map shows that there are no Ca-rich terrestrial veins in the vicinity of this grain, and none that correlate with the morphology of the altered cores. (Msk = maskelynite, Ol = olivine, Px = pyroxene, lv. = level of X-ray intensity normalized to current and dwell time).

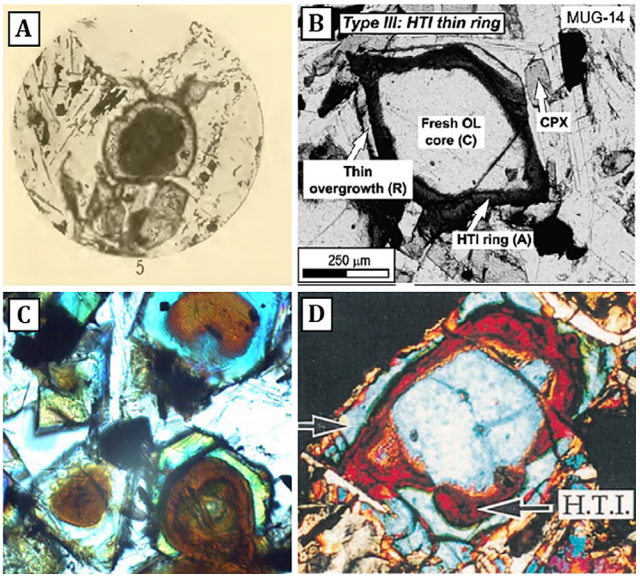

Fig. 11. Terrestrial examples of deuterically altered olivine. (A) Thin section of a basalt from Colorado (after Ross and Shannon, 1925). (B) Olivine from the Barque de Hiro gabbroic intrusion, from Maupiti Island (Society archipelago, French Polynesia; after Clément et al., 2007). (C) Cross-polarized light image of deuterically altered olivine grains from the La Jara Creek Basalt in Southern Colorado (after Vaci et al., 2020). (D) Olivine collected from the bottom of a 6 m thick basalt flow, Eiao, Marquesas (after Caroff et al., 2000). (HTI = high temperature iddingsite, CPX = clinopyroxene, OL = olivine).

water dissociating into H_2 and O_2 (Herd et al., 2002; Herd, 2003). Hydrogen is preferentially exsolved from the magma and eventually lost to the atmosphere (Herd et al., 2002), temporarily increasing the oxidation state of the magma resulting in the alteration of the early formed olivine cores. Once the degassing process has ceased, the groundmass

minerals and fayalitic olivine overgrowths will crystallize from this residual melt under more reducing conditions (Goff, 1996; Caroff et al., 1997; Caroff et al., 2000; Clément et al., 2007).

Evidence of extensive degassing within HTI-bearing rocks is supported by the vesicle-rich segregation structures these basalts and gabbros are associated with such as vesicle cylinders, vesicle sheets, and pegmatoids formed by the ascent of low-density residual liquid plumes that have differentiated from their water-rich lava or magma hosts (Goff, 1996; Caroff et al., 1997; Caroff et al., 2000; Clément et al., 2007). The volatile release during this segregation process allows for the groundmass olivine and overgrowth rims to crystallize without being affected by HTI alteration (Goff, 1996; Caroff et al., 1997; Caroff et al., 2000; Clément et al., 2007). The terrestrial basalts noted here are also finely vesicular, supporting the escape of gases (Ross and Shannon, 1925; Edwards, 1938; Goff, 1996; Caroff et al., 1997; Caroff et al., 2000; Clément et al., 2007; Vaci et al., 2020). Vesicles were not observed in NWA 7042 or 10416, but it is possible that the advance of the crystallization front in the magma was slower than the bubble velocity, allowing the vesicles to migrate upward without freezing in the lower solidified rock that formed these martian samples (Caroff et al., 1997). Due to the lower atmospheric pressure and gravity on Mars the ascending magma will also degas more efficiently, lowering the chances of freezing in the vesicles upon cooling (Herd et al., 2002).

Geochemical evidence in NWA 7042 and NWA 10416 also points to a two-stage crystallization sequence similar to the deuterically altered terrestrial basalts. In both samples the olivine core compositions (in NWA 7042 $\sim Fo_{69.7}$) are markedly out of equilibrium with the bulk-rock Mg#'s (57.9 in NWA 7042) for any plausible values of $K_{Dol\text{-}melt}^{Fe\text{-}Mg}$ (e.g., Filiberto and Dasgupta, 2011), suggesting that the olivine cores formed under different conditions to the olivine rims and late-stage Fe-rich unaltered olivines. Qualitatively, the oxide assemblages in NWA 7042 show a trend of increasing oxygen fugacity (fO_2) with crystallization between the cores and late stage olivines/rims. The Mg-rich, Ti-poor chromites within the olivine cores indicates that their initial crystallization occurred in low fO_2 conditions. The composition of the Cr-bearing spinels evolved to more Fe^{3+} and Ti-rich compositions as crystallization progressed and fO_2 increased, culminating in the crystallization of late-stage titanomagnetite and ilmenite grains observed in association with maskelynite, ferropigeonite, and merrillite. The same oxidation trend is observed in NWA 10416 (Herd et al., 2016; Vaci et al., 2020). The altered olivine core margins in both samples likely formed as a result of the temporary increase in oxidation conditions that occurred after water saturation and prior to degassing of the residual melt. Studies on terrestrial samples use the occurrence of HTI assemblages, such as laihunite, as evidence of this temporary fO_2 increase (Goff, 1996; Caroff et al., 2000; Clément et al., 2007). As previously mentioned, Mg-laihunite has also been observed in NWA 10416 (Vaci et al., 2020). Other evidence for late stage increases in fO_2 includes exsolution lamellae within spinel (Fig. 12). Similar spinel exsolution lamellae textures have been observed in several other martian meteorites and are thought to have formed via late-stage episode(s) of oxidation (Herd et al., 2001; Herd et al., 2002; Goodrich et al., 2003). The compositions of the lamellae within the spinels are difficult to resolve by quantitative analysis as they are generally too fine, but they are typically interpreted as exsolution of ilmenite or ulvöspinel (Goodrich et al., 2003). We were unable to carry out quantitative fO_2 calculations in NWA 7042 as the majority of the spinels and ilmenite are either extensively weathered and cracked, contain exsolution lamellae, and/or contain significant amounts of Al and Mg (4 wt.% Al_2O_3, 2 wt.% MgO in spinel, and 2.5 wt.% MgO in ilmenite; Table 1). Because these compositions deviate significantly from "ideal" Fe-Ti oxides it is difficult to use conventional models to calculate meaningful fO_2 values (Herd et al., 2001). In terrestrial samples the formation of HTI stops when oxygen fugacity drops below the FMQ (Fayalite–Magnetite–Quartz) buffer (Goff, 1996; Clément et al., 2007). This is consistent with our qualitative fO_2 estimates of the groundmass which are all well below FMQ; however, it should be noted that exsolution lamellae are also observed within some spinel grains along the rims of the fayalitic olivine rims, meaning there may have been multiple late stage episodes of oxidation.

Late-stage magmatic alteration via residual melts and fluids on Mars (i.e. deuteric alteration) has also been proposed as a possible formation mechanism for high-temperature alteration phases observed in olivine and pyroxene-hosted melt inclusions within several nakhlites (McCubbin et al., 2009; Filiberto et al., 2014), as well as iddingsite alteration of poikilitically enclosed olivine in shergottite ALH 77005 (Kuebler, 2013). It has also been suggested that the Fe- and Mg-rich clays that dominate the Noachian terrains of Mars formed by deuteric alteration via residual, water-rich magma-derived fluids within cooling basaltic magma bodies (Meunier et al., 2012). While these meteorite and remote sensing studies point to widespread deuteric alteration on Mars, NWA 7042 has also been subjected to significant terrestrial weathering during its residence time in the desert on Earth. As such, the possibility that terrestrial weathering processes formed the alteration within the olivine cores must also be considered.

4.1.3. Weathering on Earth

Determining the origin of mineral alteration (i.e. whether it is deuteric or meteoric) is difficult as both types of processes can be superimposed (Delvigne et al., 1979). For example, in terrestrial rocks deuteric alteration can later weather to iron oxide products through meteoric alteration once the olivine is at or near Earth's surface (Delvigne et al., 1979). In addition, both low- and high-temperature iddingsite form in similar ways, with alteration fronts beginning at the rims of olivine crystals (that are typically more Fe-rich) progressing inwards along cracks and crystallographically controlled planes (Delvigne et al., 1979; Smith et al., 1987; Wilson, 2004).

The mineral assemblages associated with surficial, post-magmatic weathering of olivine include mixtures of hydrous iron and magnesium silicates such as goethite,

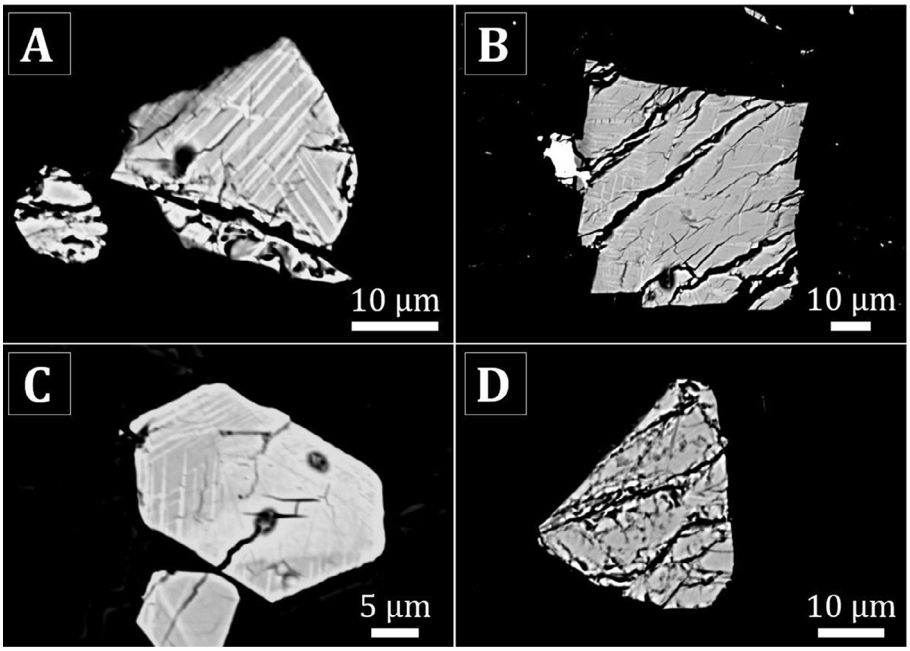

Fig. 12. BSE images of Cr-Fe-Ti rich spinels in NWA 7042 olivine. (A), (B), and (D) were observed within olivine cores, and (C) was observed closer to the rim. The spinel in (D) has been extensively weathered and cracked. The lighter colored lamellae are inferred to be ilmenite based on similarities with other martian meteorites, and slightly lower Cr concentrations observed via EDS.

montmorillonite, smectite, illite, and chlorite (Gay and Lemaitre, 1961; Clément et al., 2007). However, several of these minerals can also be ascribed to high-temperature deuteric and metamorphic alteration complicating this even further (Delvigne et al., 1979; Eggleton, 1984; Smith et al., 1987; Banfield et al., 1990; Wilson, 2004). Due to the complex nature of these weathering/alteration mixtures, TEM is typically needed to identify them. In NWA 7042, we were not able to identify any of these low temperature minerals from our preliminary TEM analysis of the altered core and core margin. However, it is possible that the Al-rich features identified in the olivine may be terrestrial as Al mobilization is typically associated with the dissolution of feldspar and glass during surficial weathering (Delvigne et al., 1979; Wilson, 2004). On the other hand, high concentrations of Al have also been observed in deuterically altered, un-weathered olivine on Earth (Goff, 1996; Caroff et al., 1997; Caroff et al., 2000; Clément et al., 2007; Vaci et al., 2020). As stated previously, the displacement of these Al-rich features along possible shock-produced fractures makes determining their origin even more complicated. At this time, we are unable to confidently state whether the observed dissolution and Al-rich features are terrestrial or martian in origin.

The ubiquitous presence of terrestrial calcite/barite weathering veins that crosscut the olivine grains in NWA 7042 and 10416 confirms that both samples have been subjected to significant terrestrial meteoric weathering. In NWA 10416, TEM analysis of olivine adjacent to a shock vein revealed undisturbed clay minerals, indicating that at least some of the alteration occurred post-shock (Piercy et al., 2020). Oxygen isotope analysis of the olivine cores in NWA 10416 may also show a mixture of martian and terrestrial reservoir signatures (Piercy et al., 2020). In NWA 7042, the yellow staining of the groundmass olivine and olivine rims, versus the pristine colorless olivine rims in NWA 10416 suggests that the effects of terrestrial weathering are even more pervasive. Evidence of terrestrial weathering is abundant in NWA 7042, and in some cases, the Mg-rich cores appear darker in olivine grains that are in closer proximity to shock veins and closer to the exterior of the sample, indicating that terrestrial overprinting may be more significant in these areas.

A recent study on NWA 10416 argues that a terrestrial weathering origin for the brown olivine cores is more likely, citing that Mg-rich olivine may be more susceptible to alteration by low-temperature surface fluids in oxidizing conditions – conditions that these finds may have been subjected to in the desert on Earth (Piercy et al., 2020). This contradicts previous work on the weathering of terrestrial olivine that shows fayalite will weather faster than forsterite due to the large ionic radius of Fe^{2+} relative to Mg^{2+}, resulting in longer and weaker bonds between Fe^{2+} and oxygen within olivine, in addition to being more susceptible to oxidation (Velbel, 1999). However, for NWA 10416 it is argued that Mg-rich olivine may have weathered faster than Fe-rich olivine based on Fe-K X-ray absorption near edge spectroscopy (XANES) data collected across an altered olivine grain within the meteorite, and previous experimental data on olivine dissolution rates (Piercy et al., 2020). XANES analysis of NWA 10416 olivine shows that Fe in the altered core margins is predominantly ferric, with ferrous Fe in the pristine rims, and intermediate ferric Fe concentrations in the cores (Piercy et al., 2020). This

enrichment trend in ferric Fe within the cores (highest at the core margin) is used as evidence that the alteration took place in an oxidizing environment that preferentially oxidized the Mg-rich cores (Piercy et al., 2020). While this oxidizing environment may be a desert on Earth, this oxidation trend is also what would be expected if the olivine cores were altered deuterically on Mars due to a temporary increase of fO_2 within the residual melt caused by degasing of volatiles (Section 4.1.2; Goff, 1996; Caroff et al., 2000; Clément et al., 2007; Tschegg et al., 2010). Deuteric alteration would also explain why Fe in the fayalitic rims is almost completely ferrous as these rims would have formed in more reducing conditions (Section 4.1.2; Goff, 1996; Caroff et al., 2000; Clément et al., 2007; Tschegg et al., 2010). Olivine dissolution rate experiments cited in the NWA 10416 study also show that Fe-rich olivine will dissolve faster than Mg-rich olivine in anoxic, reducing conditions (Wogelius and Walther, 1992; Hausrath and Brantley, 2010), but these experimental studies do not provide context on what would be expected in an oxygen-rich terrestrial desert on Earth (Piercy et al., 2020). It is noted that as appropriate experimental data of olivine reactivity under low-temperature oxidizing conditions is lacking there is a great deal of uncertainty, and that this allows for the possibility that Mg-rich olivine may be more reactive than Fe-rich olivine in terrestrial desert conditions (Piercy et al., 2020). While there is uncertainty in terms of experimental data, if forsteritic olivine does weather more easily than more fayalitic compositions then this type of alteration zoning in other martian meteorite finds from the desert should be observed. In contrast, significantly weathered martian meteorites such as DaG 476 and 489 (with olivine zoned from Fo_{76} cores to Fo_{56} rims) show low-temperature iddingsite weathering on the more fayalitic rims, even though cracks and fractures are abundant in olivine (Crozaz and Wadhwa, 2001; Mikouchi et al., 2001). In NWA 7042 and NWA 10416 we would also expect to see the heaviest alteration in areas of highest Mg concentrations (i.e. the center of the olivine cores $Fo_{60.8\text{-}76.1}$). Instead, the heaviest alteration occurs along the core margins which are slightly more fayalitic (Table 1). In addition, the Mg contents of the altered olivine core margins also overlap with the unaltered rim overgrowths (alteration rim = $Fo_{54.4\text{-}69.9}$, overgrowth = $Fo_{41.0\text{-}68.83}$).

Whereas we contest the idea that Mg-rich olivine will weather faster than Fe-rich olivine in a desert environment on Earth, it is possible that a higher density of planar shock features in the olivine cores could allow for more terrestrial weathering in these areas. In rare instances, brown alteration phases were observed along the planar fractures within the olivine cores (Fig. 13). These planar fractures are observed in both the fayalitic rims and altered cores,

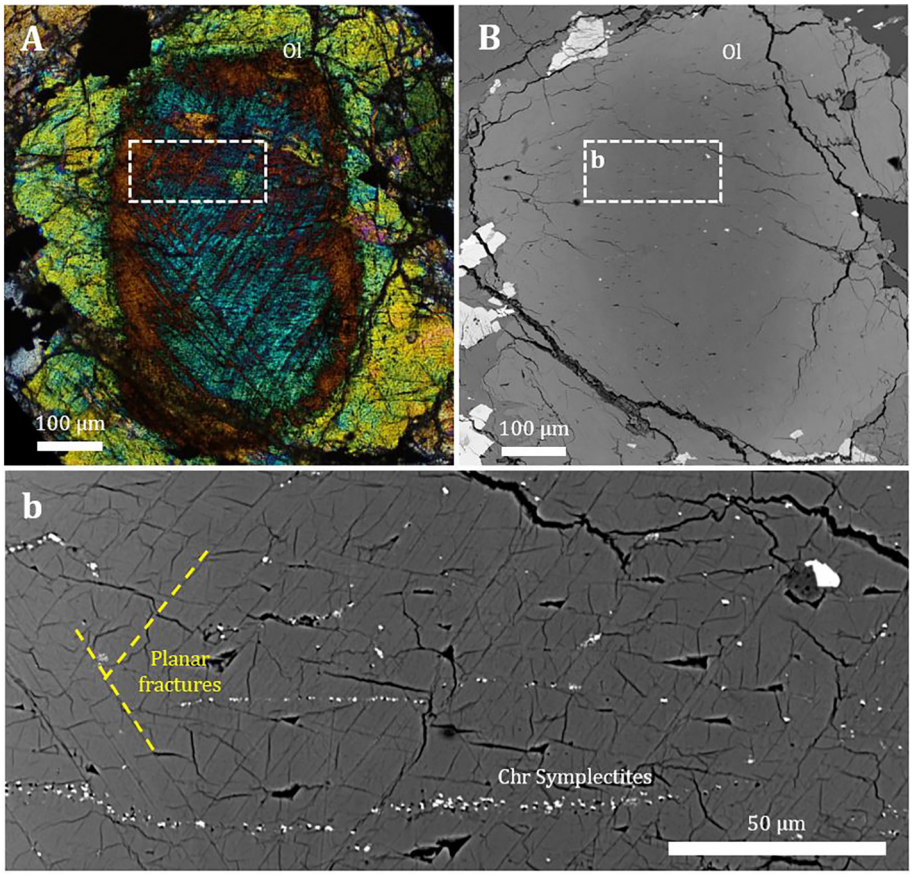

Fig. 13. Cross-polarized light (A) and BSE (B) images of an olivine grain with in-filled planar features. (b) Close-up view of the planar fractures, with the two main directions highlighted in yellow for ease of viewing. (Ol = olivine, Chr = chromite). (For interpretation of the references to colour in this figure legend, the reader is referred to the web version of this article.)

but are more pervasive in the cores relative to the rims. If these are shock-produced planar features, then the infilling of alteration phases indicates overprinting by weathering post-shock (likely on Earth). The alteration associated with the planar features is slightly enriched in Ca and Al and appears to originate from the altered core margins progressing inwards towards the center of the grain. If the core margins were magmatically altered on Mars, the amorphization and increased porosity in these areas could have allowed for terrestrial water to more easily infiltrate into the planar fractures in contact with them. It is unclear why there are more planar features observed within the core than the rim in these rare cases. It may be possible that Mg-rich olivine is more susceptible to shock than the Fe-rich olivine, although we could not find any previous work to support this (i.e. Stöffler et al., 2018). Instead, it may be that the already altered olivine cores were more susceptible to shock than the un-altered rims, resulting in different densities of planar features, or that these planar features developed in-situ due to cooling rather than shock. As this infilling of planar features is not observed in the majority of the altered olivine cores (Fig. 3), infiltration by terrestrial water is unlikely to be the cause of the alteration zoning, but it cannot be ruled out. The alteration around the core margin could also possibly be explained by a lattice misfit between the Fe-rich rim and Mg-rich core resulting in periodic edge dislocations along this boundary (Smith et al., 1987). More analysis is needed to identify the alteration phases within the core margins and along these fractures, but as evidence of terrestrial overprinting is ubiquitous across the sample, it will be difficult to identify any high-temperature deuteric alteration phases that still persist.

4.2. Igneous crystallization sequence

Based on the mineral chemistry, oxygen fugacity, petrology, and alteration occurrence in NWA 7042, the following crystallization history is proposed (see Figs. S5–S8 in Supplementary Materials 1 for more detail):

(1) The parental magma of NWA 7042 formed by partial melting (and possibly mixing) in the mantle and intruded into the martian crust, ponding at depth.
(2) As the magma cooled, chromite and Mg-rich olivine cores began to crystallize. As chromite grains are commonly enclosed within the forsteritic olivine cores it is inferred that chromite crystallized prior to or synchronously with olivine.
(3) If the olivine were altered deuterically, the concentration of H_2O in the residual melt would have increased as it was excluded from the growing crystals. When the magma began to ascend, pressure decreased and the volatiles in the residual melt began to degas resulting in a dramatic increase in fO_2 (likely above the NNO buffer; Goff, 1996; Caroff et al., 1997; Caroff et al., 2000; Herd et al., 2002; Clément et al., 2007). This temporary increase in fO_2 led to the alteration of the olivine cores and produced assemblages of laihunite intergrowths, magnetite, and silica within the cores and core margins (Banfield et al., 1990; Goff, 1996). As these minerals were not identified in NWA 7042 it is possible that terrestrial weathering on Earth may have overprinted and/or destroyed these assemblages.
(4) As the magma continued to ascend and sufficient quantities of volatiles were released, fO_2 decreased and the alteration reaction was reversed resulting in the crystallization of the Fe-rich olivine rims, Fe-rich groundmass olivine, and Mg-rich pigeonite cores.
(5) As the magma continued to cool, sub-calcic augite rims grew over the Mg-rich pigeonite cores to form the zoned pyroxene laths. This was followed by the crystallization of the remainder of the groundmass within the interstices of the pyroxene laths including plagioclase, ferropigeonite, merrillite, apatite, titanomagnetite, ilmenite, pyrrhotite, and baddeleyite.

4.3. Shock metamorphism

Following crystallization, NWA 7042 was ejected due to an impact event approximately 2 m.y. (Huber et al., 2013) resulting in the amorphization of plagioclase to maskelynite, fracturing of olivine and pyroxene, and the formation of shock veins.

4.3.1. Maskelynite

The sector zoning observed in CL images of maskelynite (Fig. S3 in Supplementary Materials 1) may have been inherited from the igneous plagioclase precursor. CL activity is greater in zones with lower BSE signal, perhaps indicating that traces of a heavy element in the maskelynite are 'quenching' the CL emission. This suggests incorporation of trace Fe into the maskelynite, as trace levels of Fe are known to be incorporated into plagioclase (Bryan, 1974). Compositional analysis of NWA 7042 maskelynite areas with different CL activities reveals that the relationship between CL emission and chemical composition is complex; however; the anorthite content and the proportions of divalent cations (Ca^{2+}, Mg^{2+}, Fe^{2+}, Mn^{2+}) to alkalis correlates with the intensity of CL emission (Fig. S6 in Supplementary Materials 1). The high concentrations of Fe, Mg, and Mn may correspond to minor melting and incorporation of surrounding phases (i.e. olivine and pyroxene) into the plagioclase during the impact event. Nano- to micron-scale inclusions of these phases in maskelynite have been previously reported in other martian meteorites including GRV 99027 (Wang and Chen, 2006), NWA 4797 (Walton et al., 2012), and NWA 6342 (White et al., 2018b; Kizovski et al., 2019).

4.3.2. High-pressure minerals

The presence of high-pressure phases in meteorites can be used to provide quantitative estimates of the minimum pressures experienced during an impact event (Baziotis et al., 2013; Walton et al., 2014). The high-pressure phases identified here require minimum pressures of 18 GPa (ringwoodite), 19 GPa (dissociation of olivine to silicate perovskite), and 10 GPa (tuite) (Xie et al., 2013; Walton

et al., 2014). These high-pressure minerals are restricted to melt veins which crosscut the primary igneous minerals. Except for the minerals in direct contact with the shock vein, the chemical zoning profiles within olivine and pyroxene appear to retain their primary igneous textures and chemical features, demonstrating that the high temperatures and pressures within the shock veins do not reflect the shock conditions experienced by the bulk rock. The preservation of these high-pressure minerals (which requires rapid cooling), indicates that the shock vein must have quenched quickly.

4.3.3. Shock pressure constraints

The shock features in olivine, pyroxene, and maskelynite (undulatory extinction and pervasive fracturing of olivine and pyroxene, and the amorphization of feldspar) indicate shock pressures of approximately 30–35 GPa (Stöffler et al., 1991; Fritz et al., 2017). The presence of shock veins suggests localized temperatures reached 1,500–1,750 °C with a minimum pressure of 19 GPa (needed to form the observed high-pressure phases). EBSD analysis of baddeleyite grains reveal poorly diffracting (quasi-amorphous) domains which have previously been associated with the partial to complete transformation and reversion of the high pressure orthorhombic-ZrO_2 phase, which forms above ~5 GPa (Darling et al., 2016; White et al., 2018a).

4.4. Implications of deuteric alteration on Mars

The altered olivine cores in NWA 7042 may represent the third petrological observation of deuteric alteration of olivine on Mars (the others being ALH 77005, and NWA 10416; Kuebler, 2013; Herd et al., 2016; Vaci et al., 2020). These three meteorites do not appear to have originated from the same source, having different ITE signatures (NWA 7042 is intermediate, ALH 77005 and NWA 10416 are depleted; Tait and Day, 2018; Herd et al., 2016), different CRE ages (~2 m.y. for NWA 7042, and ~1 m.y. for NWA 10416; Huber et al., 2013; Cassata et al., 2016), and significantly different petrology (Herd et al., 2016). Evidence of deuterically altered olivine in these three unique samples implies that deuteric alteration by water within martian magmas could be a more ubiquitous process than previously assumed.

Deuteric alteration during late-stage crystallization has also been proposed as a way to explain the elevated water contents and δD within olivine in Tissint (Hallis et al., 2017). The lack of alteration phases observed in Tissint olivine is explained by insufficient water available for deuteric alteration to progress beyond the initial stages (Hallis et al., 2017). Based on this, NWA 7042, NWA 10416, and ALH 77005 may originate from comparatively water-rich sources; or magmas that ascended quickly enough to maintain water oversaturation prior to degassing (Caroff et al., 2000). In addition to the shergottites listed here, deuteric alteration of feldspar within olivine and pyroxene-hosted melt pockets has been previously observed in the nakhlites (McCubbin et al., 2009; Filiberto et al., 2014). In the case of the nakhlites, the Cl-rich alteration phases are believed to have formed from the alteration of feldspar by fluids exsolved from a Cl-rich parent magma with low H_2O-activity (Filiberto et al., 2014).

Electron microprobe results show that the altered cores in NWA 7042 are similar to the high Al, low total analyses collected from the alteration phases in NWA 10416, ALH 77005, nakhlite NWA 817, and terrestrial analogues (Caroff et al., 2000; Gillet et al., 2001; Clément et al., 2007; Kuebler, 2013; Vaci et al., 2020). In these cases the alteration assemblages did not contain considerable F, Cl, or C, and were likely produced via water-rich fluids either from within the magma source, or exogenous metasomatic or hydrothermal fluids (Caroff et al., 2000; Gillet et al., 2001; Clément et al., 2007; Kuebler, 2013; Vaci et al., 2020). There is abundant evidence of significant water in the shergottites' source magmas. Water measurements from martian apatites indicate that the water content of the martian mantle is similar to the volatile content of the terrestrial mid-ocean ridge basalt mantle sources; and the shergottites' parent magmas (which formed via partial melting of this water-rich mantle source) are estimated to have had 139–2870 ppm H_2O prior to degassing (McCubbin et al., 2012; Gross et al., 2013; Filiberto et al., 2016; McCubbin et al., 2016).

5. SUMMARY AND CONCLUSIONS

- Northwest Africa 7042 is comprised of two generations of olivine (early zoned olivine Fo_{41-76}, and late-stage fayalitic olivine Fo_{46-56}), euhedral to subhedral clinopyroxene (pigeonite with sub-calcic augite overgrowths), and intersertal maskelynite laths associated with ferropigeonite. Accessory phases include merrillite, apatite, titanomagnetite, chromite, ilmenite, pyrrhotite and baddeleyite. These igneous phases are crosscut and displaced by shock veins, which are in turn crosscut by terrestrial weathering veins of calcite and barite.
- Northwest Africa 7042 contains unique alteration features distinct from the majority of other shergottites, but similar to deuterically altered basalts and gabbros (via magmatic fluids) on Earth. The cores of the zoned olivine grains have been pervasively altered resulting in rusty-brown stained cores with dark-brown margins, surrounded by significantly less altered yellow to colorless overgrowth rims. The presence of un-altered rims surrounding the altered cores suggests that the alteration of the cores took place at magmatic temperatures prior to crystallization of the rims on Mars. Crosscutting relationships between shock veins and the altered olivine also indicate that the alteration occurred prior to the shock event on Mars. However, the presence of alteration phases in-filling shock-produced planar fractures within the olivine cores complicates this theory. As no high-temperature phases were able to be identified a terrestrial origin for the alteration cannot be ruled out.
- Shock-related metamorphism includes the transformation of feldspar to maskelynite, pervasive fracturing in olivine and pyroxene, planar fractures in olivine,

poorly-diffracting (quasi-amorphous) baddeleyite, and the formation of melt-rich shock veins containing high-pressure polymorphs. Bulk melting and high-pressure polymorphs are restricted to launch-generated melt veins.

The large recovered mass of NWA 7042 makes it an ideal subject for isotopic and geochronological studies, particularly regarding alteration on Mars, the origin of diversity in shergottite magmas, and corresponding heterogeneities in martian geochemical reservoirs through time.

Declaration of Competing Interest

The authors declare that they have no known competing financial interests or personal relationships that could have appeared to influence the work reported in this paper.

ACKNOWLEDGEMENTS

T.V.K. acknowledges the Hatch University Graduate Fund and the support of the Natural Sciences and Engineering Research Council of Canada (NSERC; funding reference #CGSD2 - 534938 – 2019). M.R.M.I thanks the Hatch foundation for financial support. We acknowledge that this study was facilitated by an NSERC Discovery Grant awarded to K.T.T. and are grateful to the Louise Hawley Stone Charitable Trust for supporting the acquisition of the NWA 7042 sample. STEM analysis was performed using EMSL (grid.436923.9), a DOE Office of Science User Facility sponsored by the Office of Biological and Environmental Research (project ID: 50780). J.M.D.D. acknowledges the NASA Solar System Workings program (NNX16AR95G). Thanks to Dr. Ana Černok, Veronica Di Cecco, Ian Nicklin, and Zoltan Vaci for discussions. We also thank Jörg Fritz, and our anonymous reviewers for their extremely helpful and constructive comments which significantly improved this manuscript; as well as Chris Herd and Jeffrey Catalano for editorial handling.

APPENDIX A. SUPPLEMENTARY MATERIAL

Supplementary data to this article can be found online at https://doi.org/10.1016/j.gca.2020.05.030.

REFERENCES

Banfield J. F., Veblen D. R. and Jones B. F. (1990) Transmission electron microscopy of subsolidus oxidation and weathering of olivine. *Contrib. Mineral. Petrol.* **106**, 110–123.

Barrat J. A., Gillet P., Sautter V., Jambon A., Javoy M., Copel C., Lesourd M., Keller F. and Petit E. (2002) Petrology and chemsitry of the basaltic shergottite North West Africa 480. *Meteorit. Planet. Sci.* **37**, 487–499.

Baziotis I. P., Liu Y., DeCarli P. S., Jay Melosh H., McSween H. Y., Bodnar R. J. and Taylor L. A. (2013) The Tissint Martian meteorite as evidence for the largest impact excavation. *Nat. Commun.* **4**, 1404–1407.

Borg L. E. and Draper D. S. (2003) A petrogenetic model for the origin and compositional variation of the martian basaltic meteorites. *Meteorit. Planet. Sci.* **38**, 1713–1731.

Brandon A. D., Puchtel I. S., Walker R. J., Day J. M. D., Irving A. J. and Taylor L. A. (2012) Evolution of the martian mantle inferred from the ^{187}Re-^{187}Os isotope and highly siderophile element abundance systematics of shergottite meteorites. *Geochim. Cosmochim. Acta* **76**, 206–235.

Bryan W. B. (1974) Fe-Mg relationships in sector-zoned submarine basalt plagioclase. *Earth Planet. Sci. Lett.* **24**, 157–165.

Cassata W. S., Hilton C., Borg L. E. and Agee C. (2016) Noble gas systematics of martian meteorite Northwest Africa 10416 (abstract #381). 26th Goldschmidt Conf.

Caroff M., Ambrics C., Maury R. C. and Cotten J. (1997) From alkali basalt to phonolite in hand-size samples: Vapor-differentiation effects in the Bouzentès lava flow (Cantal, France). *J. Volcanol. Geotherm. Res.* **79**, 47–61.

Caroff M., Maury R. C., Cotten J. and Clément J. P. (2000) Segregation structures in vapor-differentiated basaltic flows. *Bull. Volcanol.* **62**, 171–187.

Clément J. P., Caroff M., Dudoignon P., Launeau P., Bohn M., Cotten J., Blais S. and Guille G. (2007) A possible link between gabbros bearing High Temperature Iddingsite alteration and huge pegmatoid intrusions: The Society Islands, French Polynesia. *Lithos* **96**, 524–542.

Connolly H. C., Smith C., Benedix G., Folco L., Righter K., Zipfel J., Yamaguchi A. and Chennaoui Aoudjehane H. (2008) The Meteoritical Bulletin, No. 93. Meteorit. Planet. Sci. 43, 583.

Crozaz G. and Wadhwa M. (2001) The terrestrial alteration of saharan shergottites dar al gani 476 and 489: A case study of weathering in a hot desert environment. *Geochim. Cosmochim. Acta* **65**, 971–977.

Darling J. R., Moser D. E., Barker I. R., Tait K. T., Chamberlain K. R., Schmitt A. K. and Hyde B. C. (2016) Variable microstructural response of baddeleyite to shock metamorphism in young basaltic shergottite NWA 5298 and improved U-Pb dating of Solar System events. *Earth Planet. Sci. Lett.* **444**, 1–12.

Day J. M. D., Corder C. A., Rumble D., Assayag N., Cartigny P. and Taylor L. A. (2015) Differentiation processes in FeO-rich asteroids revealed by the achondrite Lewis Cliff 88763. *Meteorit. Planet. Sci.* **50**, 1750–1766.

Day J. M. D., Tait K. T., Udry A., Moynier F., Liu Y. and Neal C. R. (2018) Martian magmatism from plume metasomatized mantle. *Nat. Commun.* **9**, 4799.

Delvigne J., Stoops G., Bisdom E. B. A. and Sleeman J. (1979) Olivines, their pseudomorphs and secondary products. *Pedologie* **29**, 247–309.

Dreibus G., Jochum K. P., Palme H., Spettel B., Wlotzka F. and Wänke H. (1992) LEW 88516: A meteorite compositionally close to the "Martian mantle." Meteoritics, 216.

Edwards A. B. (1938) The formation of Iddingsite. *Am. Mineral.* **23**, 277–281.

Eggleton R. A. (1984) Formation of iddingsite rims on olivine: a transmission electron microscope study. *Clays Clay Miner.* **32**, 1–11.

Filiberto J., Gross J. and McCubbin F. M. (2016) Constraints on the water, chlorine, and fluorine content of the Martian mantle. *Meteorit. Planet. Sci.* **51**, 2023–2035.

Filiberto J., Treiman A. H., Giesting P. A., Goodrich C. A. and Gross J. (2014) High-temperature chlorine-rich fluid in the martian crust: A precursor to habitability. *Earth Planet. Sci. Lett.* **401**, 110–115.

Filiberto J., Chin E., Day J. M. D., Franchi I. A., Greenwood R. C., Gross J., Penniston-Dorland S. C., Schwenzer S. P. and Treiman A. H. (2012) Geochemistry of intermediate olivine-phyric shergottite Northwest Africa 6234, with similarities to basaltic shergottite Northwest Africa 480 and olivine-phyric shergottite Northwest Africa 2990. *Meteorit. Planet. Sci.* **47**, 1256–1273.

Filiberto J. and Dasgupta R. (2011) Fe2+-Mg partitioning between olivine and basaltic melts: Applications to genesis of olivine-phyric shergottites and conditions of melting in the Martian interior. *Earth Planet. Sci. Lett.* **304**, 527–537.

Fritz J. and Greshake A. (2009) High-pressure phases in an ultramafic rock from Mars. *Earth Planet. Sci. Lett.* **288**, 619–623.

Fritz J., Greshake A. and Fernandes V. A. (2017) Revising the shock classification of meteorites. *Meteorit. Planet. Sci.* **52**, 1216–1232.

Gay P. and Lemaitre R. W. (1961) Some observation on "iddingsite". *Am. Mineral.* **46**, 92–111.

Giannuzzi L. A. and Stevie F. A. (1999) A review of focused ion beam milling techniques for TEM specimen preparation. *MICRON* **30**(3), 197–204. https://doi.org/10.1016/S0968-4328(99)00005-0.

Gillet P., Barrat J. A., Crozaz G., Deloule E., Jambon A., Neuville D., Sautter V. and Wadhwa M. (2001) Aqueous alteration in the NWA 817 martian meteorite. *Meteorit. Planet. Sci.* **36**, A66.

Goff F. (1996) Vesicle cylinders in vapor-differentiated basalt flows. *J. Volcanol. Geotherm. Res.* **71**, 167–185.

Goodrich C. A., Herd C. D. K. and Taylor L. A. (2003) Spinels and oxygen fugacity in olivine-phyric and lherzolitic shergottites. *Meteorit. Planet. Sci.* **38**, 1773–1792.

Gross J., Filiberto J. and Bell A. S. (2013) Water in the martian interior: Evidence for terrestrial MORB mantle-like volatile contents from hydroxyl-rich apatite in olivine-phyric shergottite NWA 6234. *Earth Planet. Sci. Lett.* **369**, 120–128.

Hallis L. J., Huss G. R., Nagashima K., Taylor G. J., Stöffler D., Smith C. L. and Lee M. R. (2017) Effects of shock and Martian alteration on Tissint hydrogen isotope ratios and water content. *Geochimica et Cosmochimica Acta* **200**, 280–294. https://doi.org/10.1016/j.gca.2016.12.035.

Hausrath E. M. and Brantley S. L. (2010) Basalt and olivine dissolution under cold, salty, and acidic conditions: What can we learn about recent aqueous weathering on Mars? *J. Geophys. Res. E: Planets* **115**(12), 1–15. https://doi.org/10.1029/2010JE003610.

Herd C. D. K. (2003) The oxygen fugacity of olivine-phyric martian basalts and the components within the mantle and crust of Mars. *Meteorit. Planet. Sci.* **1805**, 1793–1805.

Herd C. D. K., Borg L. E., Jones J. H. and Papike J. J. (2002) Oxygen fugacity and geochemical variations in the martian basalts: implications for martian basalt petrogenesis and the oxidation state of the upper mantle of Mars. *Geochim. Cosmochim. Acta* **66**, 2025–2036.

Herd C. D. K., Papike J. J. and Brearley A. J. (2001) Oxygen fugacity of martian basalts from electron microprobe oxygen and TEM-EELS analyses of Fe-Ti oxides. *Am. Mineral.* **86**, 1015–1024.

Herd C. D. K., Walton E. L., Ziegler K., Vaci Z., Agee C. B., Muttik N., Wimpenny J., Cassata W. S. and Borg L. E. (2016) The Northwest Africa 10416 Olivine-phyric Martian Basalt: Product of Magma Mixing, Assimilation and Alteration (abstract #2527). 47th Lunar Planet. Sci. Conf.

Huber L., Irving A. J., Maden C. and Wieler R. (2013) Noble gas cosmic ray exposure ages for five shergottites and evidence for trapped martian atmosphere in tissint (abstract #1534). 44th Lunar Planet. Sci. Conf.

Irving A. J., Kuehner S. M., Chen G., Herd C. D. K., Tanaka R. and Lapen T. J. (2012) Petrologic, Elemental and Isotopic Characterization of Two Unusual Martian Meteorites: Depleted Permafic Microgabbroic Shergottite Northwest Africa 7032 and Intermediate Permafic Intersertal Shergottite Northwest Africa 7042 (abstract #2496). 43rd Lunar Planet. Sci. Conf.

Izawa M. R. M., Tait K. T., Moser D. E., Barker I. R., Hyde B. C., Nicklin R. I. and Lapen T. J. (2015) Mineralogy, petrology and geochronology of intermediate shergottite NWA 7042 (abstract #2523). 46th Lunar Planet. Sci. Conf.

Kayama M., Sekine T., Tomioka N., Nishido H., Kato Y., Ninagawa K., Kobayashi T. and Yamaguchi A. (2018) Cathodoluminescence of high-pressure feldspar minerals as a shock barometer. *Meteorit. Planet. Sci.* **53**, 1476–1488.

Kizovski T. V., Tait K. T., Di Cecco V. E., White L. F. and Moser D. E. (2019) Detailed mineralogy and petrology of highly shocked poikilitic shergottite Northwest Africa 6342. *Meteorit. Planet. Sci.* **54**, 768–784.

Kuebler K. E. (2013) A comparison of the iddingsite alteration products in two terrestrial basalts and the Allan Hills 77005 martian meteorite using Raman spectroscopy and electron microprobe analyses. *J. Geophys. Res. E Planets* **118**, 803–830.

Laetsch T. A. and Downs R. T. (2006) Software for identification and refinement of cell parameters from powder diffraction data of minerals using the RRUFF Project and American Mineralogist Crystal Structure Databases (abstract). 19th Gen. Meet. Int. Mineral. Assoc.

Lafuente B., Downs R. T., Yang H. and Stone N. (2015) The power of databases: The RRUFF project. Highlights mineral. *Crystallogr.*, 1–30.

Lee M. R., Tomkinson T., Hallis L. J. and Mark D. F. (2015) Formation of iddingsite veins in the martian crust by centripetal replacement of olivine: Evidence from the nakhlite meteorite Lafayette. *Geochim. Cosmochim. Acta* **154**, 49–65.

Lodders K. (1998) A survery of shergottite, nakhlite and chassigny meteorites whole-rock compositions. *Meteorit. Planet. Sci.* **33**, A183–A190.

McCubbin F. M., Boyce J. W., Srinivasan P., Santos A. R., Elardo S. M., Filiberto J., Steele A. and Shearer C. K. (2016) Heterogeneous distribution of H_2O in the Martian interior: Implications for the abundance of H_2O in depleted and enriched mantle sources. *Meteorit. Planet. Sci.* **51**, 2036–2060.

McCubbin F. M., Hauri E. H., Elardo S. M., Vander Kaaden K. E., Wang J. and Shearer C. K. (2012) Hydrous melting of the martian mantle produced both depleted and enriched shergottites. Geology 40, 683–686.

McCubbin F. M., Tosca N. J., Smirnov A., Nekvasil H., Steele A., Fries M. and Lindsley D. H. (2009) Hydrothermal jarosite and hematite in a pyroxene-hosted melt inclusion in martian meteorite Miller Range (MIL) 03346: Implications for magmatic-hydrothermal fluids on Mars. *Geochim. Cosmochim. Acta* **73**, 4907–4917.

McDonough M. F. and Sun S. S. (1995) The Composition of the Earth. *Chem. Geol.* **120**, 223–253.

McSween H. Y. (2015) Petrology on Mars. *Am. Mineral.* **100**, 2380–2395.

McSween H. Y. and Treiman A. H. (1998) Martian meteorites. *Planet. Mater.* **36**.

Meunier A., Petit S., Ehlmann B. L., Dudoignon P., Westall F., Mas A., El Albani A. and Ferrage E. (2012) Magmatic precipitation as a possible origin of Noachian clays on Mars. *Nat. Geosci.* **5**, 739–743.

Mikouchi T., Miyamoto M. and McKay G. A. (2001) Mineralogy and petrology of the Dar al Gani 476 martian meteorite: Implications for its cooling history and relationship to other shergottites. *Meteorit. Planet. Sci.* **36**, 531–548.

Moser D. E., Chamberlain K. R., Tait K. T., Schmitt A. K., Darling J. R., Barker I. R. and Hyde B. C. (2013) Solving the Martian meteorite age conundrum using micro-baddeleyite and launch-generated zircon. *Nature* **499**, 454–457.

Noguchi T., Nakamura T., Misawa K., Imae N., Aoki T. and Toh S. (2009) Laihunite and jarosite in the Yamato 00 nakhlites: Alteration products on Mars? *J. Geophys. Res. E Planets* **114**.

Nyquist L. E., Bogard D. D., Greshake A. and Eugster O. (2001) Ages and geologic histories of Martian meteorites. *Chronol. Evol. Mars* **96**, 105–164.

Ostertag R., Amthauer G., Rager H. and McSween H. Y. (1984) Fe^{3+} in shocked olivine crystals of the ALHA 77005 meteorite. *Earth Planet. Sci. Lett.* **67**, 162–166.

Piercy J. D., Bridges J. C., Hicks L. J., Macarthur J. L., Greenwood R. C. and Franchi I. A. (2020) Terrestrial alteration mineral assemblages in the NWA 10416 olivine phyric shergottite. *Geochim. Cosmochim. Acta* **280**, 26–45. https://doi.org/10.1016/j. gca.2020.03.026.

Pouchou J.-L. and Pichoir F. (1991) Quantitative Analysis of Homogeneous or Stratified Microvolumes Applying the Model "PAP." In Electron Probe Quantitation Springer US. pp. 31–75.

Ross C. S. and Shannon E. V. (1925) The origin, occurrence, composition, and physical properties of the mineral iddingsite. *Proc. United States Natl. Museum* **67**, 1–19.

Shearer C. K., Burger P. V., Papike J. J., McCubbin F. M. and Bell A. S. (2015) Crystal chemistry of merrillite from Martian meteorites: Mineralogical recorders of magmatic processes and planetary differentiation. *Meteorit. Planet. Sci.* **50**, 649–673.

Shearer C. K., Aaron P. M., Burger P. V., Guan Y., Bell A. S. and Papike J. J. (2013) Petrogenetic linkages among fO2, isotopic enrichments-depletions and crystallization history in Martian basalts. Evidence from the distribution of phosphorus in olivine megacrysts. *Geochim. Cosmochim. Acta* **120**, 17–38.

Shearer C. K., Burger P. V., Papike J. J., Borg L. E., Irving A. J. and Herd C. (2008) Petrogenetic linkages among Martian basalts: Implications based on trace element chemistry of olivine. *Meteorit. Planet. Sci.* **43**, 1241–1258.

Smith D. K. and Newkirk W. (1965) The crystal structure of baddeleyite (monoclinic ZrO2) and its relation to the polymorphism of ZrO_2. *Acta Crystallogr.* **18**, 983–991.

Smith K. L., Milnes A. R. and Eggleton R. A. (1987) Weathering of basalt: formation of iddingsite. *Clays Clay Miner.* **35**, 418–428.

Stöffler D., Keil K. and Edward R. D. (1991) Shock metamorphism of ordinary chondrites. *Geochim. Cosmochim. Acta* **55**, 3845–3867.

Stöffler D., Hamann C. and Metzler K. (2018) Shock metamorphism of planetary silicate rocks and sediments: Proposal for an updated classification system. *Meteorit. Planet. Sci.* **53**, 5–49.

Tait K. T. and Day J. M. D. (2018) Chondritic late accretion to Mars and the nature of shergottite reservoirs. *Earth Planet. Sci. Lett.* **494**, 99–108.

Takenouchi A., Mikouchi T. and Yamaguchi A. (2018) Shock veins and brown olivine in Martian meteorites: Implications for their shock pressure–temperature histories. *Meteorit. Planet. Sci.* **53**, 2259–2284.

Treiman A. H., Dyar M. D., McCanta M., Noble S. K. and Pieters C. M. (2007) Martian Dunite NWA 2737: Petrographic constraints on geological history, shock events, and olivine color. *J. Geophys. Res. E Planets* **112**, 1–20.

Treiman A. H. (2003) Chemical compositions of martian basalts (shergottites): some inferences on basalt formation, mantle metasomatism, and differentiation on Mars. *Meteorit. Planet. Sci.* **38**, 1849–1864.

Treiman A. H., Barrett R. A. and Gooding J. L. (1993) Preterrestrial aqueous alteration of the Lafayette (SNC) meteorite. *Meteoritics* **28**, 86–97.

Tschauner O., Ma C., Beckett J. R., Prescher C., Prakapenka V. B. and Rossman G. R. (2014) Discovery of bridgmanite, the most abundant mineral in Earth, in a shocked meteorite. *Science* **6213**, 1100–1102.

Tschegg C., Ntaflos T., Kiraly F. and Harangi S. (2010) High temperature corrosion of olivine phenocrysts in Pliocene basalts from Banat, Romania. Austrian. *J. Earth Sci.* **103**, 101–110.

Usui T., Sanborn M., Wadhwa M. and McSween H. Y. (2010) Petrology and trace element geochemistry of Robert Massif 04261 and 04262 meteorites, the first examples of geochemically enriched lherzolitic shergottites. *Geochim. Cosmochim. Acta* **74**, 7283–7306.

Vaci Z., Agee C. B., Herd C. K. D., Walton E., Tschauner O., Ziegler K., Prakapenka V. P., Greenberg E. and Monique-Thomas S. (2020) Hydrous olivine alteration on mars and earth. *Meteorit. Planet. Sci.*. https://doi.org/10.1111/maps.13479.

Velbel M. A. (1999) Bond strength and the relative weathering rates of simple orthosilicates. *Am. J. Sci.* **299**, 679–696.

Wadhwa M. (2001) Redox state of Mars' upper mantle and crust from Eu anomalies in shergottite pyroxenes. *Science* **291**, 1527–1530.

Walton E. L., Irving A. J., Bunch T. E. and Herd C. D. K. (2012) Northwest Africa 4797: A strongly shocked ultramafic poikilitic shergottite related to compositionally intermediate Martian meteorites. *Meteorit. Planet. Sci.* **47**, 1449–1474.

Walton E. L., Sharp T. G., Hu J. and Filiberto J. (2014) Heterogeneous mineral assemblages in martian meteorite Tissint as a result of a recent small impact event on Mars. *Geochim. Cosmochim. Acta* **140**, 334–348.

Wang D. and Chen M. (2006) Shock-induced melting, recrystallization, and exsolution in plagioclase from the Martian lherzolitic shergottite GRV 99027. *Meteorit. Planet. Sci.* **41**, 519–527.

White L. F., Darling J. R., Moser D. E., Cayron C., Barker I., Dunlop J. and Tait K. T. (2018a) Baddeleyite as a widespread and sensitive indicator of meteorite bombardment in planetary crusts. *Geology* **46**, 719–722.

White L. F., Kizovski T. V., Tait K. T., Langelier B., Gordon L. M., Harlov D. and Norberg N. (2018b) Nanoscale chemical characterisation of phase separation, solid state transformation, and recrystallization in feldspar and maskelynite using atom probe tomography. *Contrib. Mineral. Petrol.* **173**.

Wilson M. J. (2004) Weathering of the primary rock-forming minerals: processes, products and rates. *Clay Miner.* **39**, 233–266.

Wogelius R. A. and Walther J. V. (1992) Olivine dissolution kinetics at near-surface conditions. *Chem. Geol.* **97**(1–2), 101–112. https://doi.org/10.1016/0009-2541(92)90138-U.

Xie X., Minitti M. E., Chen M., Mao H.-K., Wang D., Shu J. and Fei Y. (2003) Tuite, γ-$Ca_3(PO_4)_2$: a new mineral from the Suizhou L6 chondrite. *Eur. J. Mineral.* **15**, 1001–1005.

Xie X., Zhai S., Chen M. and Yang H. (2013) Tuite, γ-$Ca_3(PO_4)_2$, formed by chlorapatite decomposition in a shock vein of the Suizhou L6 chondrite. *Meteorit. Planet. Sci.* **48**, 1515–1523.

Zhai S. M., Wu X. A. and Ito E. (2010) High-pressure Raman spectra of tuite, gamma-Ca3(PO4)(2). *J. Raman Spectrosc.* **41**, 1011–1013.

Associate editor: Christopher Herd